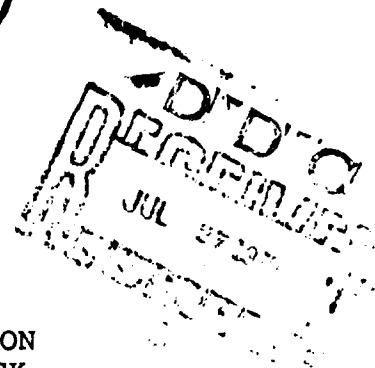


ADA071893

2/2

REPORT ONR-CR212-225-4F

LEVEL



PREDICTION OF LATERAL AERODYNAMIC LOADS ON
FIGHTER AIRCRAFT AT HIGH ANGLES OF ATTACK

S. B. Spangler
and S. C. Perkins, Jr.

Contract N00014-74-C-0344
ONR Task 212-225

31 July 1978

Final Report

Approved for public release; distribution unlimited.

DDG FILE COPY



PREPARED FOR THE

OFFICE OF NAVAL RESEARCH • 800 N. QUINCY ST. • ARLINGTON • VA • 22217

Change of Address

Organizations receiving reports on the initial distribution list should confirm correct address. This list is located at the end of the report. Any change of address or distribution should be conveyed to the Office of Naval Research, Code 211, Arlington, VA 22217.

Disposition

When this report is no longer needed, it may be transmitted to other organizations. Do not return it to the originator or the monitoring office.

Disclaimer

The findings and conclusions contained in this report are not to be construed as an official Department of Defense or Military Department position unless so designated by other official documents.

Reproduction

Reproduction in whole or in part is permitted for any purpose of the United States Government.

Unclassified

COPY NO. 13

SECURITY CLASSIFICATION OF THIS PAGE (When Data Entered)

REPORT DOCUMENTATION PAGE		READ INSTRUCTIONS BEFORE COMPLETING FORM	
1. REPORT NUMBER ONR-CR212-225-4F	2. GOVT ACCESSION NO.	3. RECIPIENT'S CATALOG NUMBER	
4. TITLE (and Subtitle) PREDICTION OF LATERAL AERODYNAMIC LOADS ON FIGHTER AIRCRAFT AT HIGH ANGLES OF ATTACK		5. TYPE OF REPORT & PERIOD COVERED Summary Technical Report	
7. AUTHOR(s) S. B./Spangler and S. C./Perkins, Jr.		6. PERFORMING ORG. REPORT NUMBER NEAR-TR-173	
9. PERFORMING ORGANIZATION NAME AND ADDRESS Nielsen Engineering & Research, Inc. 510 Clyde Avenue Mountain View, CA 94043		8. CONTRACT OR GRANT NUMBER(s) N00014-74-C-0344	
11. CONTROLLING OFFICE NAME AND ADDRESS Office of Naval Research 800 North Quincy Street Arlington, VA 22217 Attn: Code 211		10. PROGRAM ELEMENT, PROJECT, TASK AREA & WORK UNIT NUMBERS 62241N RF41-411-801.2-30 RMS1411-801	
14. MONITORING AGENCY NAME & ADDRESS (if different from Controlling Office)		12. REPORT DATE 31 July 1978	
		13. NUMBER OF PAGES	
		15. SECURITY CLASS. (of this report) Unclassified	
		15a. DECLASSIFICATION/DOWNGRADING SCHEDULE	
16. DISTRIBUTION STATEMENT (of this Report) Approved for public release; distribution unlimited.			
17. DISTRIBUTION STATEMENT (of the abstract entered in Block 20, if different from Report)			
18. SUPPLEMENTARY NOTES			
19. KEY WORDS (Continue on reverse side if necessary and identify by block number) Aerodynamic Loads Asymmetric Vortex Shedding High Angle of Attack Spin Departure			
20. ABSTRACT (Continue on reverse side if necessary and identify by block number) This report presents a brief summary of methods and experi- mental data developed over a four year period to predict the static lateral forces acting on a modern fighter-type aircraft at high angles of attack and small angles of sideslip characteristic of a departure flight attitude. Extensive reference is made to earlier reports under this contract for details of the methods and the test programs and results.			

DD FORM 1 JAN 73 1473

Unclassified

SECURITY CLASSIFICATION OF THIS PAGE (When Data Entered)

Unclassified

SECURITY CLASSIFICATION OF THIS PAGE(When Data Entered)

20. Continued

→ The major part of the report is devoted to application of the methods to two aircraft configurations on which detailed data exist, comparison of the predicted and measured results, and evaluation of the comparisons. The configurations are a research V/STOL fighter configuration and the F-5 aircraft. Comparisons are made on nose vortex positions, circulation distributions in the separated region above the nose, flow velocities in the same region, and loads on the nose alone and complete configuration.

Generally, the methods predict all of the correct behavior of these highly nonlinear and complicated flows. However, the agreement in many cases is not sufficiently good to consider the methods as satisfactory design or analysis techniques. Additional work is suggested to provide further verification and improvements. ↗

Accession For		<input checked="checked" type="checkbox"/>
NTIS GRA&I		<input type="checkbox"/>
DDC TAB		<input type="checkbox"/>
Unannounced		
Justification		
By _____		
Distribution/		
Availability Code		
Dist.	Availand/ special	

Unclassified

SECURITY CLASSIFICATION OF THIS PAGE(When Data Entered)

PREFACE

This technical report covers the work performed under Contract N00014-74-C-0344 from 1 May 1977 to 31 July 1978 and is the fourth and summary technical report published under the program.

Dr. Robert Whitehead and Mr. David S. Siegel, Office of Naval Research, were the Navy Scientific Officers.

TABLE OF CONTENTS

<u>Section</u>	<u>Page No.</u>
LIST OF ILLUSTRATIONS	4
LIST OF TABLES	6
1. INTRODUCTION	7
2. OVERALL APPROACH	8
3. METHODS OF ANALYSIS	9
3.1 Nose Vortex Shedding	9
3.2 Wing/Body/Strake Loads	13
3.3 Tail Loads	15
4. DATA SOURCES	16
4.1 Water Tunnel Tests	16
4.2 V/STOL Tunnel Tests	18
4.3 NASA F-5 Tests	21
5. COMPARISONS WITH DATA	21
5.1 Nose Alone	22
5.1.1 V/STOL configuration	22
5.1.2 F-5 configuration	42
5.2 Complete Configuration	54
5.2.1 V/STOL model	56
5.2.2 F-5A model	70
6. DISCUSSION OF RESULTS	72
7. CONCLUDING REMARKS	75
REFERENCES	76
SYMBOLS	78

LIST OF ILLUSTRATIONS

<u>Figure</u>		<u>Page</u> <u>No.</u>
1	Asymmetric vortex-shedding model for noncircular cross sections	10
2	Water tunnel model characteristics	17
3	V/STOL fighter model and rake mounted in V/STOL wind tunnel	19
4	Langley Research Center V/STOL fighter model	20
5	Predicted vortex cloud positions for V/STOL body at BS 52 for $\alpha = 35^\circ$, $\beta = 0^\circ$	24
	a) $1/2^\circ$ Asymmetric disturbance	24
	b) 2° Asymmetric disturbance	25
6	Predicted and measured circulation distribution above V/STOL body for $\alpha = 35^\circ$, $\beta = 0^\circ$	26
	a) BS 52	26
	b) BS 69	27
7.	Predicted and measured crossflow plane velocities above V/STOL body at $\alpha = 35^\circ$, $\beta = 0^\circ$, BS 52	29
	a) In vertical plane of symmetry	29
	b) Along line 18° off vertical plane	30
8	Side force and yawing moment for V/STOL nose alone at $\beta = 0$	32
9	Predicted vortex cloud positions for V/STOL body at BS 52 for $\alpha = 35^\circ$, $\beta = 10^\circ$	33
10	Predicted and measured circulation distribution above V/STOL body for $\alpha = 35^\circ$, $\beta = 10^\circ$	34
	a) BS 52	34
	b) BS 69	35
11	Predicted and measured crossflow plane velocities above V/STOL body at $\alpha = 35^\circ$, $\beta = 10^\circ$, BS 52	38
	a) In vertical plane of symmetry	38
	b) Along a line 18° off the vertical plane of symmetry	39
12	Predicted and measured side force and yawing moment coefficients on V/STOL nose at $\alpha = 35^\circ$	40

LIST OF ILLUSTRATIONS (Concluded)

Figure	Page
13 Predicted separation location on V/STOL nose at $\alpha = 35^\circ$, $\beta = 10^\circ$ for two separation criteria	41
14 Predicted vortex cloud position for F-5 nose	44
a) $\alpha = 30^\circ$, $\beta = 0^\circ$, 41 percent station	44
b) $\alpha = 40^\circ$, $\beta = 0^\circ$, 41 percent station	45
c) $\alpha = 40^\circ$, $\beta = 0^\circ$, 32 percent station	46
d) $\alpha = 30^\circ$, $\beta = -10^\circ$, 41 percent station	47
e) $\alpha = 40^\circ$, $\beta = -10^\circ$, 41 percent station	48
15 Comparison of measured and predicted vortex position for F-5 nose	50
a) $\alpha = 30^\circ$, $\beta = 0^\circ$	50
b) $\alpha = 40^\circ$, $\beta = 0^\circ$	50
c) $\alpha = 30^\circ$, $\beta = 10^\circ$	51
d) $\alpha = 40^\circ$, $\beta = 10^\circ$	51
16 Comparison of side force and yawing moment water tunnel data and theory for 41 percent length F-5 nose	52
17 Comparison of side force and yawing moment wind tunnel data and theory for 32 percent length F-5 nose	53
18 Predicted vortex positions over length of V/STOL model for $\alpha = 35^\circ$, $\beta = 0^\circ$, $\Delta\beta = -1/2^\circ$, no strakes	57
a) Nose vortex cloud fitted with two vortices	57
b) Nose vortex cloud fitted with six vortices	58
19 Measured circulation distribution over V/STOL body at wing trailing edge (BS 98) for $\alpha = 35^\circ$, $\beta = 20^\circ$, strakes off	59
20 Predicted vortex positions over length of V/STOL model for $\alpha = 35^\circ$, $\beta = 0^\circ$, $\Delta\beta = -1/2^\circ$, strakes on	62
a) Initial strake vortex height given by delta wing data	62
b) Initial strake vortex height half that given by delta wing data	63
21 Predicted vortex positions over length of V/STOL model for $\alpha = 35^\circ$, $\beta = 10^\circ$, strakes off	67
22 Measured circulation distribution over V/STOL body at wing trailing edge (BS 98) for $\alpha = 35^\circ$, $\beta = 10^\circ$, strakes off	68

LIST OF TABLES

<u>Table</u>		<u>Page</u> <u>No.</u>
I	Comparison of Predicted and Measured Side Force and Yawing Moment Coefficients for V/STOL Configuration at $\alpha = 35^\circ$ for zero sideslip	61
II	Comparison of Predicted and Measured Side Force and Yawing Moment Coefficients for V/STOL Configuration at $\alpha = 35^\circ$ for 10° sideslip	66
III	Comparison of Predicted and Measured Side Force and Yawing Moment Coefficients for F-5A	71

PREDICTION OF LATERAL AERODYNAMIC LOADS ON FIGHTER AIRCRAFT AT HIGH ANGLES OF ATTACK

1. INTRODUCTION

This is the Final Technical Report on a program conducted by Nielsen Engineering & Research, Inc. (NEAR) for the Office of Naval Research to develop engineering techniques for predicting the lateral aerodynamic load distribution on fighter-bomber aircraft at incipient departure flight conditions. The problem considered is one in which the aircraft is in the range of angle of attack (generally 30° to 45°) in which a steady asymmetric vortex system is formed on the nose. The vortices induce a side-force on the nose and pass over the wing and tail to induce a side-force on these components. This vortex system is an important source of lateral aerodynamic effects causing departure for many aircraft.

This program has been conducted over a four year period. The work of the first two years was primarily analytical. Preliminary work was done on asymmetric vortex shedding from circular cross section noses and the subsequent interaction of these vortices with the wing, body, and tail. A vortex lattice program was developed to calculate the properties of the vortices over the wing/body, to calculate the interaction of the nose and strake vortices and to calculate the loads on the wing/body in the presence of the nose and strake vortices. Tail vortex interference methods were used to calculate tail loads in the presence of the nose and wing/strake vortex systems. This work is described in reference 1. This vortex lattice program was subsequently modified to perform these calculations in the presence of small sideslip. That work is described in reference 2.

It was apparent in applying these methods to real aircraft configurations that it would be necessary to consider more realistic nose shapes, since it was becoming clear that tailoring the shape of the nose can greatly improve the aerodynamic characteristics and handling qualities of the aircraft at high angles of attack. Since no experimental work had been done on noncircular nose shapes in which flow fields and vortex positions were measured, some tests were conducted in the third year to provide guidance to analytical work on noncircular nose vortex shedding.

In addition, an analytical model was developed for noncircular nose vortex shedding. This work is summarized in reference 3.

The final year's work has been directed to analysis of the data, application of the analytical methods to the test configurations, and comparisons between predicted and measured results. This report briefly summarizes the results of the earlier work and concentrates on the data comparisons and assessments of the methods.

2. OVERALL APPROACH

The problem of interest is the flow over a high speed fighter-bomber at angles of attack in the asymmetric steady vortex-shedding range (perhaps 30° to 45°), small sideslip angles, and zero angular rates. The analysis and experiments have been limited to incompressible flow, although they can be extended to speeds up to the critical speed. The configurations of interest are nose/wing/body/strake/tail configurations typical of modern high speed aircraft. The flow is dominated by separation on the relatively sharp slender nose and leading edges of the wing and strakes. The aerodynamic loads of greatest interest are the side force and yawing moment which are strongly influenced by flow separation effects and in the case of zero sideslip are due entirely to these effects.

The general approach makes use of the body of potential flow methods that have been developed over the past 15 years or so to calculate nonlinear wing/body/tail vortex interference effects on aircraft and missiles. These methods have been used with considerable success in many kinds of configurations. They represent the important physical phenomena of the flow and provide good insight into the nature of the interference loading and yet are relatively straightforward in application.

The aircraft configuration is divided into segments for purposes of analysis: the nose, the wing/strake/body, the afterbody (if present) and tail. Methods are developed to characterize the separated flow over the nose in terms of potential vortices. In order to model the important features of the flow, a large number, or "cloud", of vortices is used. The distribution of vortices in the cloud is calculated aft to the axial station of the strake-leading-edge intersection with the fuselage.

For purposes of calculating the influence of the nose shed-vorticity on the aft surfaces of the aircraft, the cloud is modeled by a small number (two to six) of concentrated vortices. The paths of these vortices are computed over the axial extent of the wing, and the induced asymmetric flow field on the wing and body surfaces is calculated. A lifting-surface method is then used to compute the load distribution on the wing/strake in the presence of the asymmetric vortex system. Leading- and side-edge separation on the wing and strake is treated using the "vortex lift" analogy of Polhamus (ref. 4). The leading-, side-, and trailing-edge wing/strake vorticity is modeled by a number of concentrated potential vortex filaments.

The nose and wing/strake vortices are then considered to trail aft over the afterbody and tail, where they induce loads on these components. Combinations of slender body and strip methods are used to calculate the afterbody and tail loads. The loads calculated are all components except drag. Primary emphasis is given in this report to side force and yawing moment, since these are a major influence on departure.

3. METHODS OF ANALYSIS

This section describes the essential features of the methods of analysis. The purpose is to provide a basic understanding of the approach, assumptions, and limitations of the methods. Reference is made to earlier reports for details of the derivations, equations, and calculated results made to evaluate the methods. The discussion is divided into nose, wing/body, and tail methods.

3.1 Nose Vortex Shedding

The major features of the analysis for vortex shedding from a non-circular nose are shown in figure 1. The analysis uses potential flow methods and slender body theory to model the steady three-dimensional flow as an unsteady, two-dimensional problem, where time in the unsteady problem is analogous to axial distance along the nose in the three-dimensional case. The basic approach is the circular cross section model of Deffenbaugh (ref. 5), to which several features have been added.

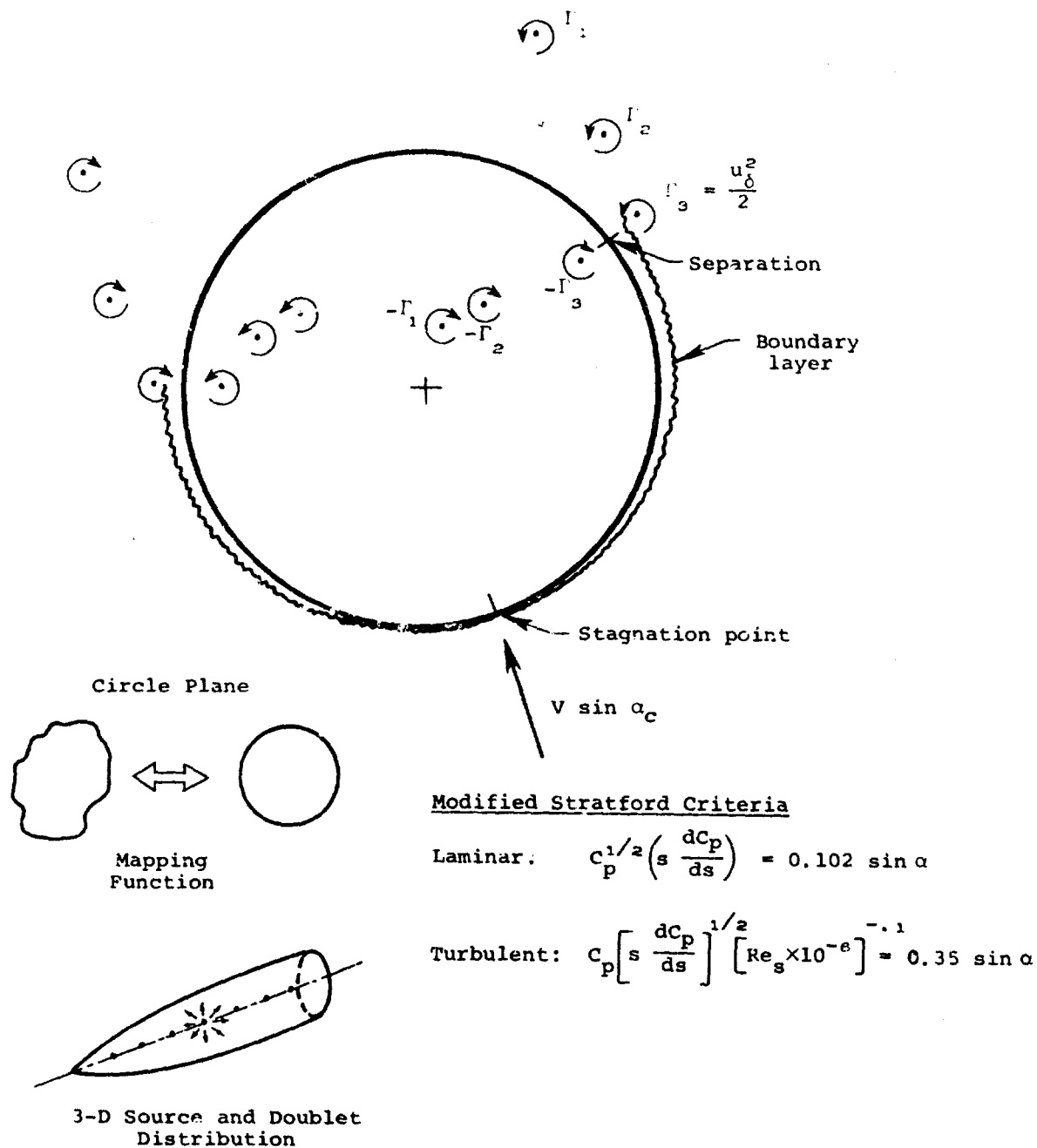


Figure 1. Asymmetric vortex-shedding model for noncircular cross sections.

Initially, a mapping function is developed to map the body cross section into a circle, using a numerical mapping scheme developed by Jameson (ref. 6) for airfoils. At a given axial station, the pressure distribution on the noncircular body is calculated in the presence of the uniform crossflow and any potential vortices that are in the flow field at that station. Velocities are calculated in the circle plane where the vortex image system can be specified and are mapped into the noncircular plane to calculate pressures. A windward stagnation point is located, and a two-dimensional boundary layer is considered to exist on either side of the body starting at the stagnation point.

In order to calculate the location of the separation points on the flanks of the body, a separation criterion based on surface pressure and run length is used. Initially, the two-dimensional Stratford criteria (ref. 7), either laminar or turbulent, were employed. These criteria depend on C_p , the gradient of C_p along the surface, a distance "s" along the surface, and for turbulent flow the Reynolds number, as shown on figure 1. Since the criteria were developed for flat-plate boundary layers subject to an adverse pressure gradient after an initial run length at constant pressure, a virtual origin is used with circular (or noncircular) bodies which provides the same displacement thickness at the minimum pressure point on the body as exists on a flat plate at the point where the adverse pressure gradient is imposed. The distance s is the distance from this virtual origin.

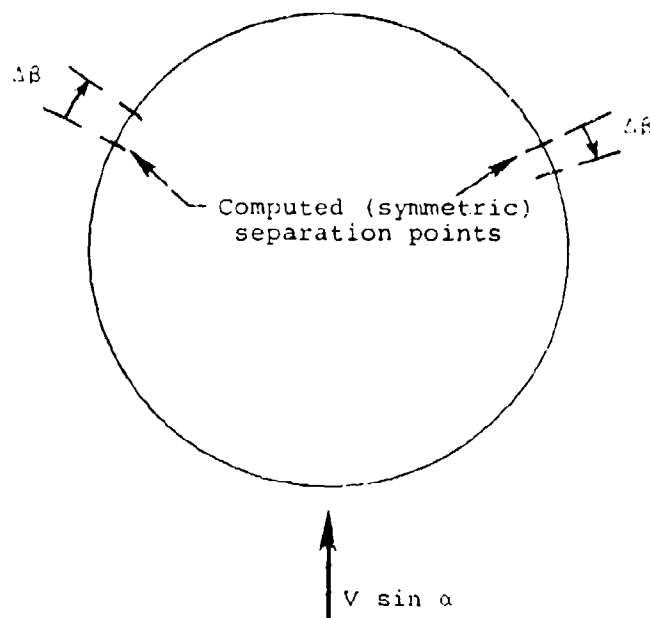
Use of these criteria on three-dimensional bodies for which measured separation line locations were available indicated that separation occurred closer to the minimum pressure location than was predicted using the criteria. Consequently a correction factor " $\sin \alpha$ " was used with the numerical Stratford criteria 0.102 and 0.35 which resulted in earlier separation and better agreement for the three dimensional case. The "modified" Stratford criteria, $0.102 \sin \alpha$ and $0.35 \sin \alpha$, shown on figure 1, were used for all calculations presented herein.

At each of the two separation points, a potential vortex is introduced a small distance off the body surface. The strength of each vortex is given by the vorticity flux in the boundary layer at separation, which depends only on the boundary-layer edge velocity. Based on empirical observations of body vortex shedding, a factor of 0.6 is applied to the

boundary layer vorticity flux to obtain the vorticity leaving the surface and entering the flow at the separation point. With increasing time (distance downstream), these vortices remain constant in strength and move away from the body along streamlines in the flow. At successive increments in time, or distance along the body, the process of calculating boundary-layer separation and introducing two vortices is repeated. Vortex positions are calculated in the circle plane and mapped into the noncircular plane.

The pressure distribution on the nose is calculated using the unsteady Bernoulli equation. In order to avoid a singularity in the velocity-potential derivative term, and improve the model of the thickness effect, a three-dimensional source distribution is used to represent the nose area distribution. Pressures are integrated to obtain loads.

For the case of a nose shape with a vertical plane of symmetry at zero sideslip, the vortex system wants to develop symmetrically, and some form of asymmetric disturbance is necessary to perturb the symmetric solution. Typically, the disturbance took the form of rotating the two computed separation points clockwise (or counterclockwise) through a small angle $\Delta\beta$ (the order of one-half degree) over the first 5 to 10 percent of the length of the nose, as shown in the sketch below. Thereafter,



the separation point locations used are those calculated from the modified Stratford criteria. The rapidity with which an appreciable asymmetry developed was found to depend on angle of attack, with little asymmetry in the shedding developing at angles of attack below about 25 degrees. For sideslip with noncircular bodies; no initial disturbance is required.

Typically about 40 pairs of vortices were used in the nose calculations for fineness ratios of about 5. Since the computer time goes up rapidly with the number of vortices, provision was made in the computer program to combine vortices. This was done on two bases. First, if two vortices got very close to each other, the two were combined into a single vortex at the "center of gravity" of the two with a strength equal to the sum of the two. Secondly, if a group in the cloud of vortices separated itself from the others, as occurs when a third vortex is formed, this group would be represented by a single vortex when the group got sufficiently far away from the body and other vortices in the cloud that its influence on the body surface pressures and the motion of the other vortices could be approximated by a single vortex. In practice, the latter option was not used in the present study.

The details of the method are described more extensively in reference 3.

3.2 Wing/Body/Strake Loads

The method for predicting loads on the portion of the aircraft between the leading- and trailing-edge wing stations has two parts. The first is a vortex lattice method for calculating loads in the presence of a given free-vortex system. The second is a crossflow plane method for locating the free vortices and calculating their induced velocities on the wing and body. The methods are described in detail in reference 2.

A vortex lattice model is used to calculate loads on the wing/body/strake at combined angles of attack and sideslip in the presence of an arbitrary asymmetric vortex system originating on the nose and passing over the configuration. The model considers arbitrary planforms having breaks in sweep on the leading and trailing edges, camber, and dihedral. The lifting surface is divided into chordwise rows of panels, with each row along the span having the same number of panels. The leading and

trailing edges of each panel correspond to constant-percent-chord lines on the wing. A horseshoe vortex is placed in each panel, with its bound leg at the quarter chord of the panel and its trailing legs along the sides of the panels. The vortices are located in the chordal plane of the wing, and the trailing legs of the horseshoe vortices are constrained to be parallel to the wing root chord, whether or not sideslip is present.

For purposes of modeling the fuselage, an equivalent circular body is defined having the same area distribution as the noncircular fuselage. An image system is used consisting of an image horseshoe vortex within the body for each horseshoe vortex on the lifting surface. The trailing legs of the image horseshoe vortices lie at the inverse points within the body. The image system is such that the wing is not required to be located vertically at the mid-height of the fuselage.

A crossflow plane analysis is used to locate the nose vortices relative to the wing/body. For this purpose, the "cloud" of vortices at the aft end of the nose is approximated with from two to six concentrated vortices whose locations are the centers of gravity of the portion of the cloud each represents. At successive axial stations, the wing/body is mapped into a circle, and the nose vortices are permitted to move along streamlines in successive crossflow planes from the wing leading to trailing edge and along the afterbody, if present. Once the locations of the nose vortices are established, induced velocities in the crossflow plane at the control points on each panel of the lifting surface are calculated. The vortex lattice solution is then calculated with these vortex-induced interference velocities added to the free stream and self-induced velocity components in the wing boundary conditions.

Leading-edge separation on the wing and strake is treated using the Polhamus vortex lift concept (ref. 4). In an initial calculation in the presence of nose vortices, the leading-edge suction is computed on the strake and wing. According to the vortex-lift concept, a portion of the suction is rotated into the normal force direction when leading-edge separation occurs. The fraction of suction rotated is a function of leading-edge sweep angle and is obtained from reference 8, based on a correlation of data mostly from delta wings.

Most of the configurations of interest have wings with leading edges that are swept less than 45 degrees and leading-edge extensions, or

strakes, that are swept at least 60 degrees. Under these circumstances, in accordance with the results of reference 8, the strake develops full vortex lift, a strake leading-edge separation vortex is formed, the wing leading edge separates but does not develop vortex lift, and the strake vortex is "torn" from the leading edge at the strake-wing junction and passes aft over the wing.

This condition is modeled in the following approximate way in the calculation method. After the first vortex-lattice calculation is made and the vortex lift known, a free strake vortex is considered to start above the wing-strake junction, and its position downstream of that point is calculated with the crossflow plane analysis, much like a nose vortex. Interaction between the strake and nose vortices occurs, which generally is significant because the strake vortices are stronger than the nose vortices. The strake vortex is assumed to originate laterally at the wing-strake junction, and the strake vortex strength is determined from the vortex span and vortex normal force calculated from the Polhamus analogy. The strake vortex height above the wing plane is chosen on the basis of observations of leading-edge separation on delta wings.

Loads are calculated on the body by locating a number of nodal points on the surface, calculating the velocity at these points, using the full Bernoulli equation to calculate pressures, and integrating over the surface area.

3.3 Tail Loads

Tail loads consist of the forces on the tail surfaces due to angles of attack and sideslip and contributions due to vortex interference from nose and wing vortices. The former are calculated using panel alone aerodynamic coefficients, from a source such as reference 9, together with the wing-body interference factors of reference 10 to account for the force carried over onto the body plus the influence of the body on the tail panel force.

Vortex interference loads are calculated using the basic approach of reference 10. The method is generalized to calculate the vortex-induced velocities along a single tail panel due to a single vortex passing over the tail, with the loads computed using a section lift-curve slope. The loads for all tail panels in the presence of all vortices are then

obtained as the sum of individual loads. The methods are described in more detail in reference 1.

4. DATA SOURCES

Several principal sources of data were used for purposes of evaluating individual aspects of the analytical methods and overall force and moment predictions. These are summarized in this section.

4.1 Water Tunnel Tests

An experimental investigation was made in the NEAR water tunnel to obtain information on vortex shedding and loads on noncircular nose shapes. Tests were conducted on three nose models, shown in figure 2, chosen to complement other parts of the investigation. One is an F-5 nose configuration, one is identical to the nose of the Langley Research Center V/STOL fighter (see section 4.2), and the third is a tangent ogive with a 1.44:1 axis ratio, elliptical cross section.

The models were mounted on a 5-component strain-gage balance which measured all force and moment components except axial force. In addition, flow visualization measurements were made to locate the vortex system relative to the nose. For this purpose, a stream of air bubbles was allowed to impinge on the windward side of the model just downstream of the nose. These bubbles streamed around the nose and flowed into the cores of the vortices, which could be located relative to the body from photographs.

The models were operated over an angle of attack range from 20 to 40 degrees and sideslip angles of 0, ± 5 , and ± 10 degrees. The water tunnel speeds varied from 1.6 m/sec to 6.1 m/sec (5 to 20 ft/sec). The loads were measured without the air bubble probe present. Flow visualization was all done at a tunnel speed of about 1.8 m/sec (6 ft/sec). Force and moment measurements were made during the flow visualization tests to determine the influence of the probe and air bubbles on the model loads.

The details of the experimental apparatus and technique and the force and moment and vortex position data are given in reference 3.

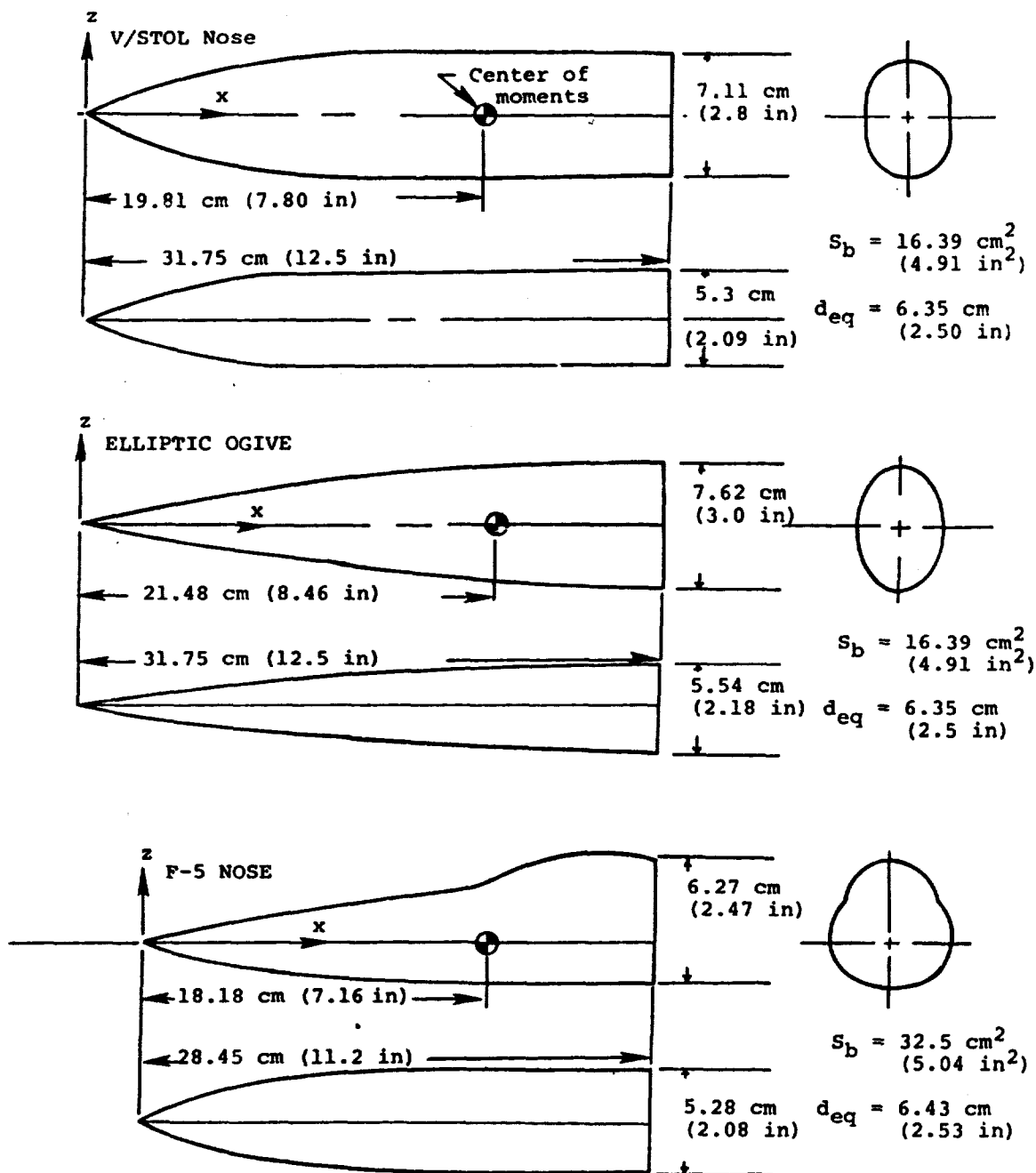


Figure 2. Water tunnel model characteristics.

4.2 V/STOL Tunnel Tests

A cooperative test program was run by the Langley Research Center, NASA, for the Office of Naval Research in support of this investigation. The tests were run in the V/STOL tunnel on an existing model of a V/STOL research fighter configuration. A photograph of the model in the tunnel is shown in figure 3.

The principal objective of the program was to obtain simultaneous measurements of both the flow field above the model and the loads on the model for a research configuration having certain essential features of a modern fighter-bomber aircraft, since no such measurements exist (at least in the available literature). Specifically, a configuration exhibiting a noncircular nose and strakes (leading-edge extensions) was desired. The results were obtained at low speeds (no compressibility effects) and at high Reynolds numbers. The data were desired for evaluating the theory on vortex shedding from noncircular cross-section, pointed noses at high angles of attack. Thus it was necessary to measure at least two components of velocity over a large enough grid to permit the vorticity field to be well defined.

The model used is an existing NASA model developed for investigating high lift features on a fighter configuration. The principal characteristics are shown in figure 4. The body has a pointed nose and a cross section consisting of two circular arcs and straight sides. The wing is a clipped delta planform with a taper ratio of 0.228, aspect ratio of 2.5, and a circular arc airfoil section. The NASA model is designed to have canards, which were not used in these tests. The canard mounts were used to support strakes, as shown by the dashed lines. The strakes have sharp leading edges and uniform thickness. An internal six component strain-gage balance was mounted within the body to measure loads.

A seven-probe rake was used to measure the flow field above the body and wing. This rake was mounted on an actuator located on the sting behind the model, as shown in figure 3. The probes were individually calibrated to measure the magnitude and direction of the onset flow up to flow angles of about 60 degrees from the probe axis (or alternately three velocity components; one along and two perpendicular to the probe axis). Scanivalves were located on the sting just aft of the actuator to record the probe pressures.



Figure 3. V/STOL fighter model and rake mounted in V/STOL wind tunnel.

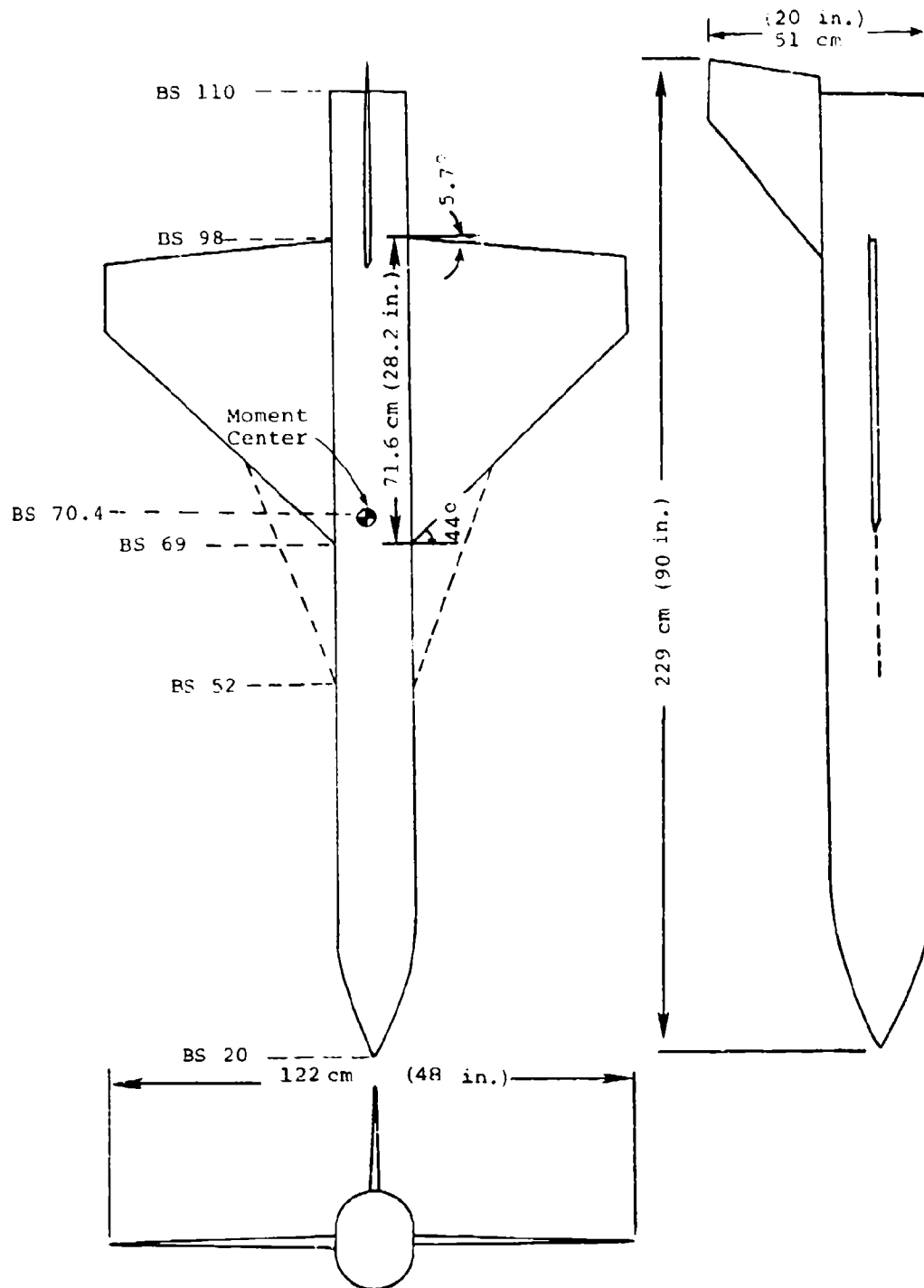


Figure 4. Langley Research Center V/STOL fighter model.

Force and moment tests were conducted initially over the range from 20° to 40° to find angles of attack at which the forces were repeatable and the nose separation vortex system appeared stable. These tests were conducted at speeds of 19 m/sec (62 ft/sec) and 60 m/sec (200 ft/sec). Based on these results, angles of attack of 20° and 35° and sideslip angles of 0° and 10° were selected for the flow field testing. The 20° case gives a symmetric vortex pattern with little side force and the 35° case gives an asymmetric vortex system with considerable side force. The flow field measurements were all obtained at speeds of about 60 m/sec.

The measurements consist of six components of forces and moments on the body and the flow field measurements. The latter were taken at 3 axial stations, shown on figure 4. The first, at Body Station (BS) 51.9, corresponds to the intersection of the strake leading edge and the body. The second, BS 69, corresponds to the intersection of the basic wing leading edge and the body and was used only with no strake present. The third, BS 98, corresponds to the intersection of the wing trailing edge and the body.

The flow field and force data are presented in reference 3, together with a more detailed description of the test program.

4.3 NASA F-5 Tests

An important source of data for this program is the series of tests that were run by NASA on a .17 scale model of the F-5 aircraft (ref. 11). Tests were run on several configurations, including nose alone, complete configuration, and the basic configuration with different wing planforms and placements. Overall forces and moments were measured in each case. The tests were run in the Full-Scale Tunnel at Langley Research Center at low dynamic pressures, such that the Reynolds numbers could be duplicated in the NEAR water tunnel.

5. COMPARISONS WITH DATA

The comparisons with data were done first for the nose vortex shedding case, because these results are an important input to the complete configuration calculation. Subsequently, calculations for the complete configurations were made. The calculations were done for the V/STOL

configuration, where the most complete set of data exists, and the F-5. The results are discussed in this section, with emphasis on the modeling of the flow phenomena as well as the comparisons of the predicted results with data.

5.1 Nose Alone

5.1.1 V/STOL configuration. - The data available for this configuration consist of forces and moments and vortex flow visualization from the water tunnel and flow field velocity distributions above the nose from the Langley wind tunnel tests. The flow conditions tested in both water and wind tunnels are $\alpha = 35^\circ$ and $\beta = 0^\circ$ and 10° . Comparisons are made on velocity and circulation distributions obtained from the wind tunnel flow field data and forces and moments.

In the prediction method, a basic source of asymmetry is present with a noncircular nose shape at combined angles of attack and sideslip, and no initial asymmetry is required in the initial conditions to develop an asymmetric vortex pattern. At zero sideslip, however, a symmetric separation vortex system will develop if the body has a vertical plane of symmetry. In this case, an asymmetric initial disturbance is required.

A number of calculations were performed to investigate the sensitivity of the predicted flow to the size and form of the asymmetric disturbance for zero sideslip. The mechanism used in all cases is a small initial asymmetric rotation either clockwise or counterclockwise of the two separation points that are calculated using the modified Stratford criterion. The first set of calculations made involved rotations of the separation points through $1/2$, 1 , and 2 degree arcs along the body for the first five integration steps along the nose, which cover approximately the initial 10 percent of the length of the nose. The water- and wind-tunnel data on forces and separated flow fields were used as a guide in assessing the results. The flow was found to be very sensitive to small disturbances at the nose, and the $1/2$ degree rotation was found to give results most closely agreeing with the data, whereas the 1 and 2 degree disturbances provided a greater asymmetry than was indicated by the data.

As a further examination of the means by which an asymmetric disturbance is created, some calculations were made in which a 2-degree shift in separation points was made over five integration steps at about

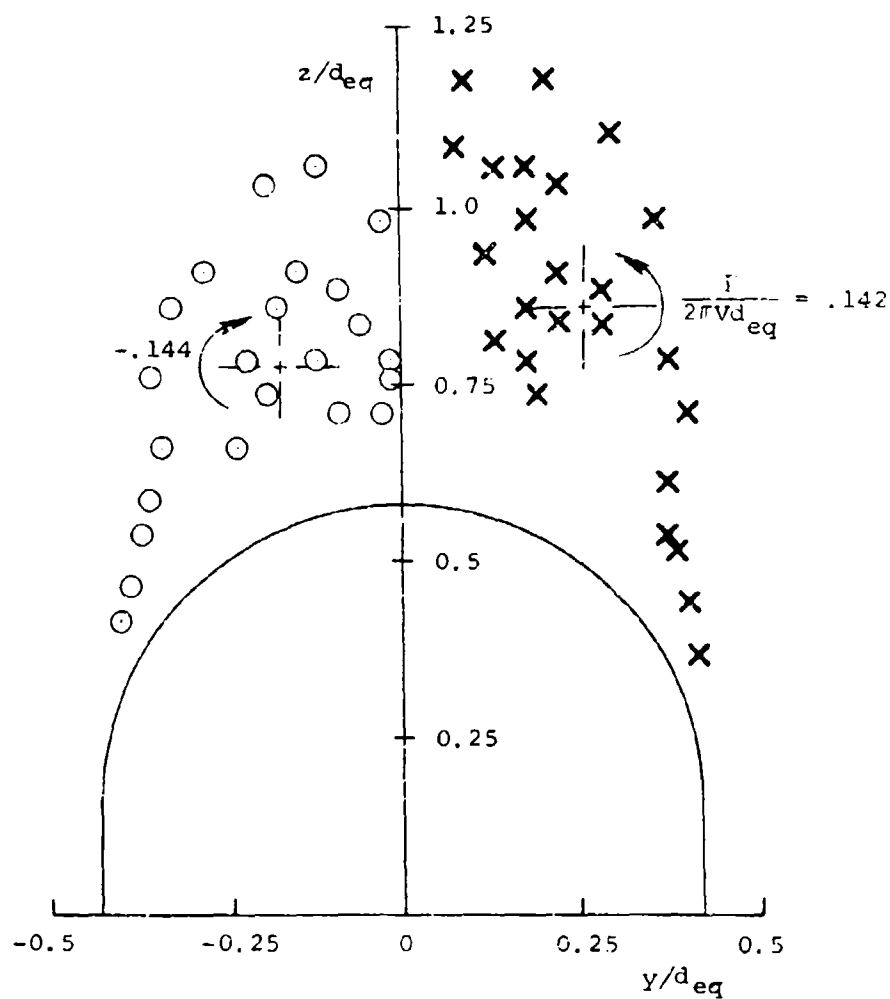
the 60 percent nose length station. This approach was based on the fact that the separation vortex pattern showed little asymmetry up to the first flow field measurement station (BS 51.9 of figure 4) and considerable development of asymmetry thereafter. Typically the (symmetric) separated flow field was well developed at this station, and a 2-degree disturbance had little influence on the downstream flow. Comparisons are presented to show this result.

Consider first the results for zero sideslip and $\alpha = 35^\circ$. The predicted distributions of vortices in the flow at BS 51.9 are shown in figures 5a and 5b for two asymmetric disturbance inputs. The 1/2-degree disturbance (fig. 5a) shows some asymmetric development, whereas the 2-degree disturbance (fig. 5b) shows very little. The values of the vorticity on each side, shown on the figures at the centers of vorticity, indicate little difference between the two cases, with the left hand or lower vortex being the stronger in both cases.

The flow-field data presented in reference 3 can be used to perform contour integrations over portions of the flow field to determine the circulation distribution in regions above the body. A direct comparison with predicted values can be obtained by summing the strengths of all the individual vortices within the same regions to obtain a predicted circulation distribution. Such a comparison is particularly useful when the vorticity is not concentrated in two small core regions, as is the case for this configuration. Some results for Body Stations 52 and 69 are shown in figures 6a and 6b.

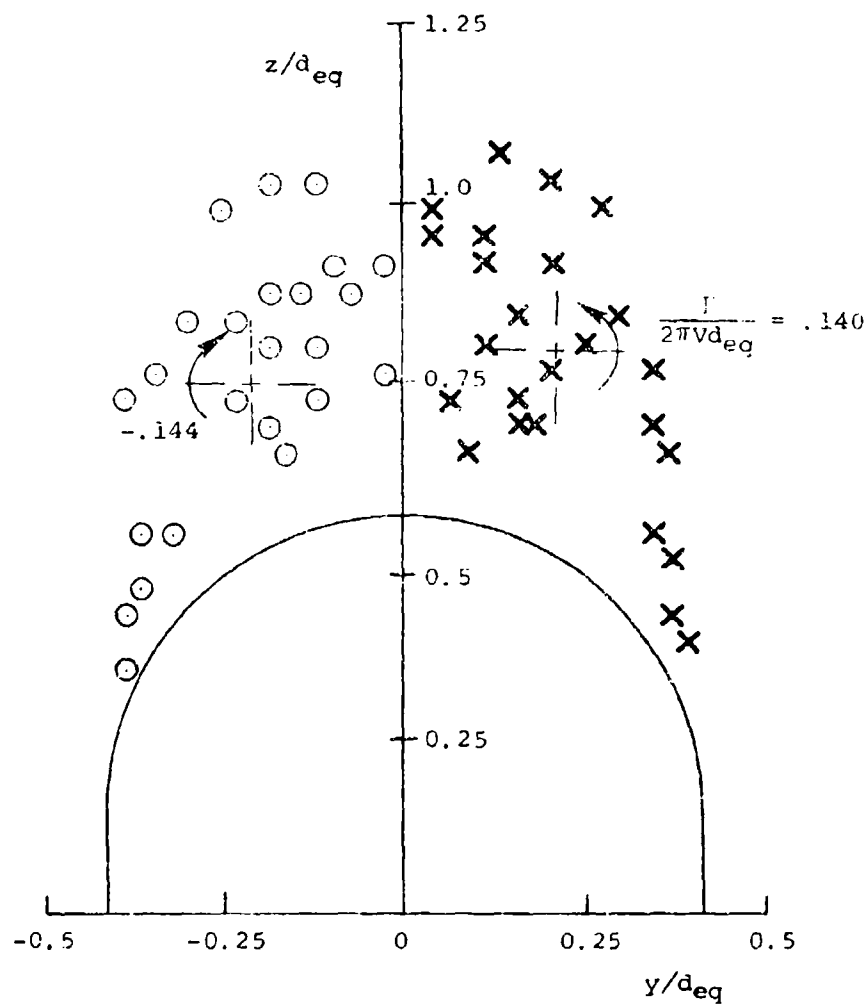
The regions are defined by the arcs that were swept by the tubes of the rake shown in figure 3. The innermost region is bounded by the arc of the lowest tube of the rake and is about 2.5cm above the body. No data were obtained between that arc and the body, although some circulation is predicted to occur in this region and is shown in figure 6. The regions are closely spaced radially near the body where the circulation is the highest and more widely spaced away from the body.

The angular boundaries between the right and left regions were selected by making contour integrations of the data over very small areas along the arcs, plotting these circulations against distance along the arcs and selecting the angular location where the circulations on the small areas changed sign. These angular boundaries were then used with



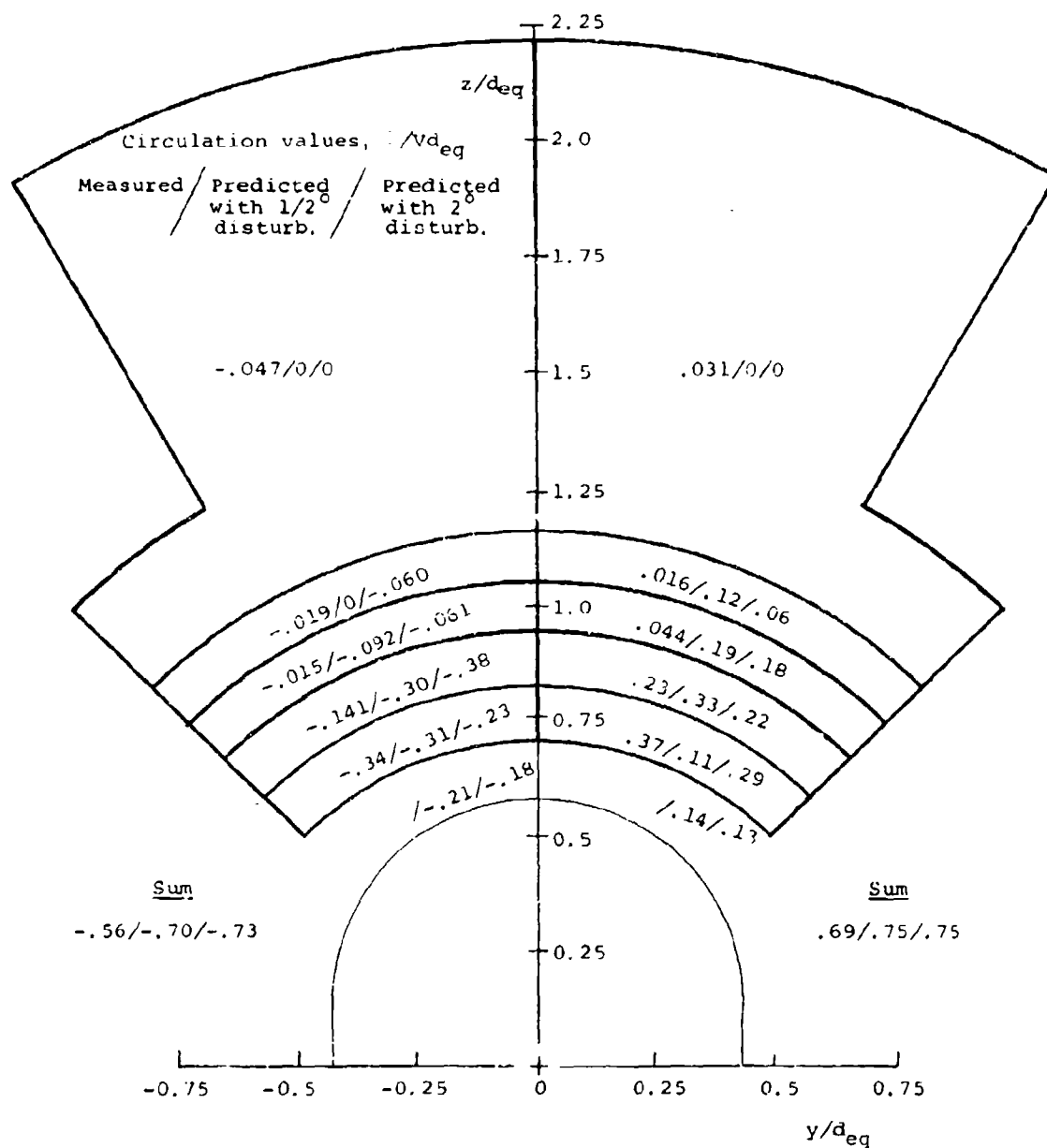
(a) $1/2^\circ$ Asymmetric disturbance.

Figure 5. Predicted vortex cloud positions for V/STOL body at BS 52 for $\alpha = 35^\circ$, $\beta = 0^\circ$.



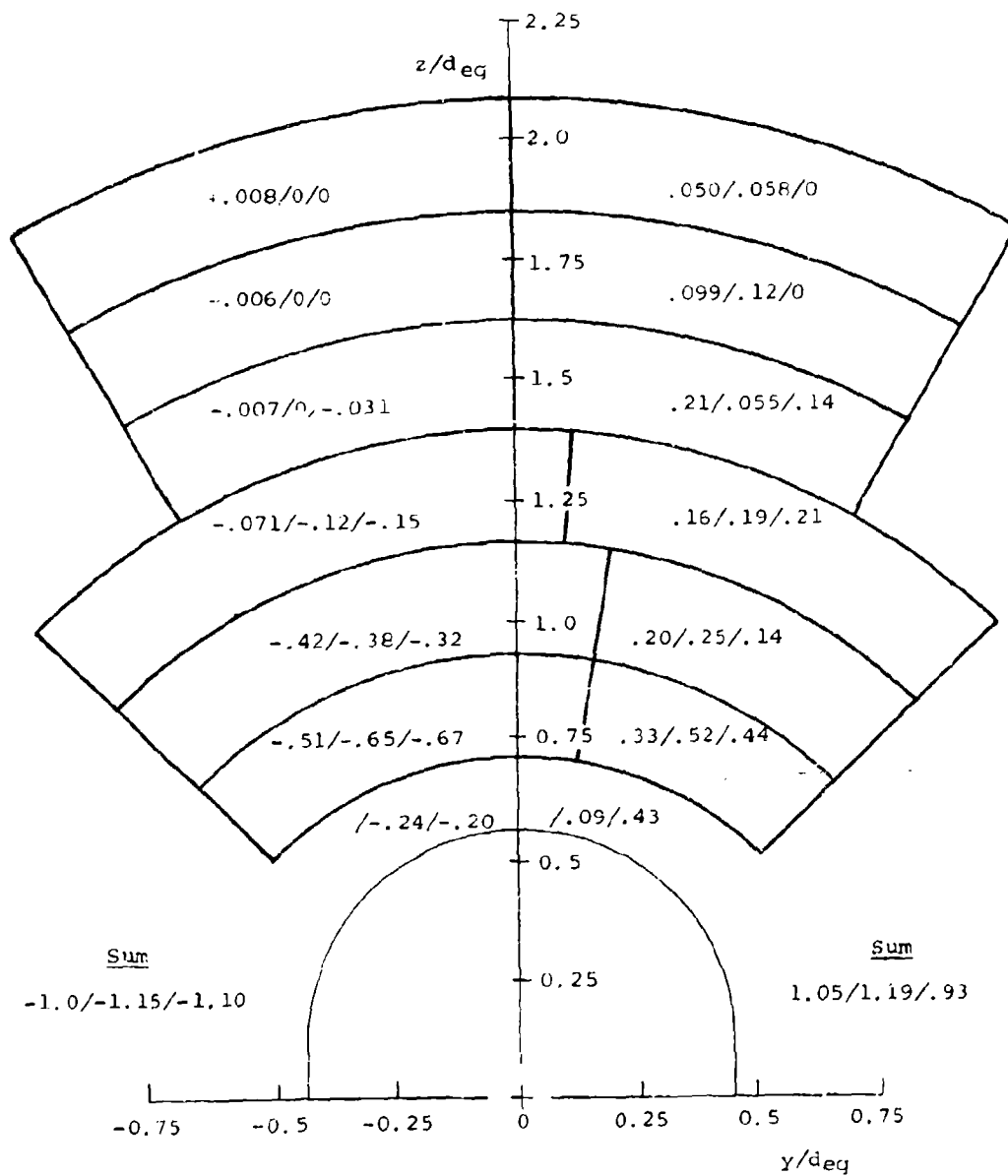
(b) 2° Asymmetric disturbance.

Figure 5. Concluded.



(a) BS 52.

Figure 6. Predicted and measured circulation distribution above V/STOL body for $\alpha = 35^\circ$, $\beta = 0^\circ$.



(b) BS = 69.

Figure 6. Concluded.

the calculated results to compare circulation distributions. For the most part, these boundaries separated both the measured and predicted positive and negative circulations reasonably well. There were some cases, however, where the boundary based on the measured results did not fit the predicted boundary well, and with positive and negative vortices summed in one region, the predicted circulations, both right and left, are low. Where important, this effect is noted.

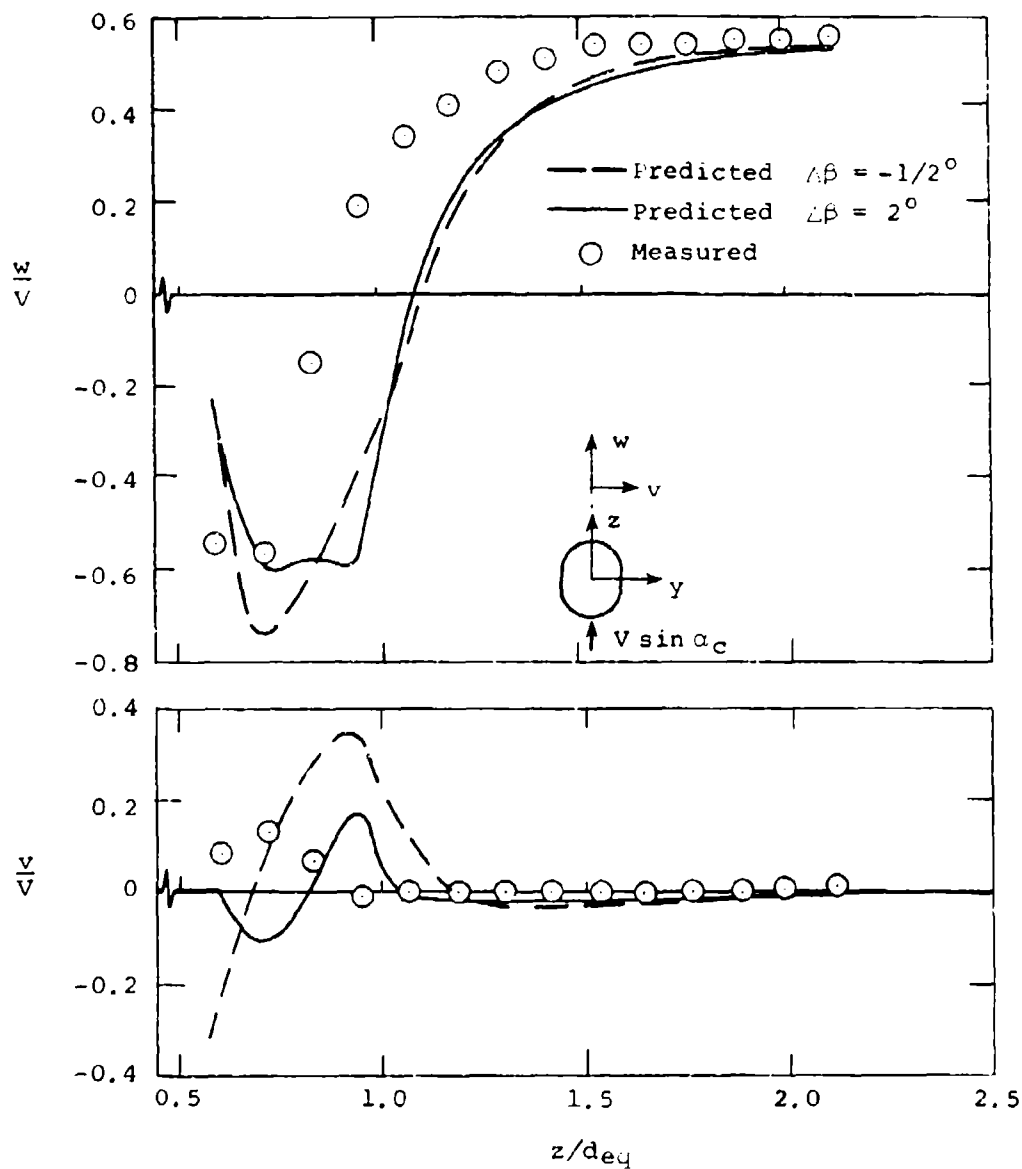
Three sets of circulations are given in figure 6 for each region. These are, in order, the measured value, the predicted value for the 1/2-degree disturbance and the predicted value for the 2-degree disturbance. For the area between the innermost region and the body, predicted circulation values are noted, but the sums of the predicted values for the positive and negative circulation do not include these predicted values closest to the body, for which no comparable measurements exist.

For BS 51.9 (fig. 6a), the two sets of predictions on the left side tend to produce too much circulation away from the body, with the 1/2-degree prediction being closer to the data. On the right side, the same trend occurs, with both predictions being similar. The predicted sums are similar and show more circulation on the right side, as does the data, but the predicted differences between right and left sides are not as great as the data indicate.

For BS 69 (fig. 6b), the two sets of predictions yield too high a circulation in the innermost region and reasonable values in the outer regions, with the 1/2-degree values being closer to the data in virtually all regions. For the 1/2-degree case, the sums show the same difference and sense of difference between the two sides, whereas the 2-degree results do not show the correct trends.

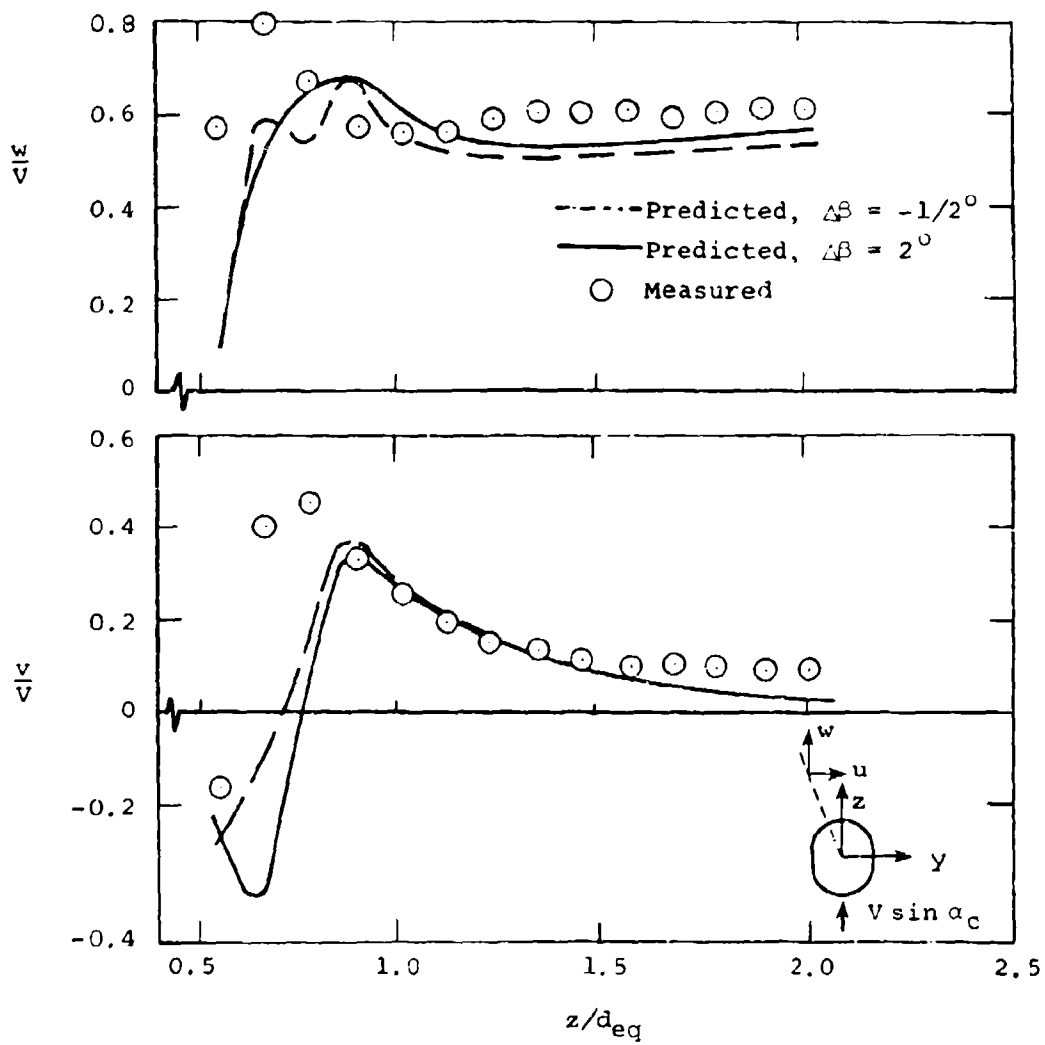
On an overall basis, the predicted circulation distributions show the same behavior as the measured values and show reasonable agreement, particularly for the downstream station which has a complex distribution of circulation.

Results for induced velocities in the region above the body at BS 52 are shown in figures 7a and 7b. Figure 7a shows induced sidewash (v/V) and upwash (w/V) along a radial line above the body in the body symmetry plane ($\theta = 90^\circ$) and figure 7b shows similar results along a line 18° from the vertical ($\theta = 108^\circ$) through the left vortex. The results shown are the data and the predictions for 1/2- and 2-degree disturbances.



(a) In vertical plane of symmetry.

Figure 7. Predicted and measured crossflow plane velocities above V/STOL body at $\alpha = 35^\circ$, $\beta = 0^\circ$, BS 52.



(b) Along line 18° off vertical plane of symmetry.

Figure 7. Concluded.

The two sets of predictions are generally very similar and show reasonable agreement with the data except in regions of high vorticity near the body. The predicted curves are irregular in some places because the points at which the velocity is calculated fall very close to a vortex, which unduly influences the contribution from that vortex. These results are typical in that the general form of the data is predicted, but no clear superiority of either prediction is evident.

A comparison of predicted side-force and yawing-moment coefficients with water tunnel measurements is shown in figure 8. The Reynolds numbers in the water tunnel correspond to the maximum tunnel velocity at which flow visualization could be obtained ($Re_D = .91 \times 10^5$) and the maximum velocity of the tunnel ($Re_D = 3.3 \times 10^5$), which still provides less than half the Reynolds number at which the wind tunnel results of figures 6 and 7 were obtained. There is a strong Reynolds number dependency shown by the water tunnel data. The 2-degree disturbance prediction shows little side force or yawing moment and agrees well with the high Reynolds number data, whereas the 1/2-degree prediction shows magnitudes approximately midway between the two Reynolds number data.

Consider now the results for 10 degrees of sideslip at $\alpha = 35^\circ$. In this case the flow is asymmetric over the body and no disturbance is necessary in the vortex shedding calculation. The predicted distribution of vortices in the flow field at BS 52 is shown in figure 9. In this case, the distribution on the leeward side is such that a group of vortices appears to be moving away from the body as a second group is forming near the separation line. This would indicate that the initial area of concentrated vorticity on the leeward side has "torn" itself from the body, and a second area is forming near the body.

This behavior is not just a mathematical quirk but appears to be a representation of the fluid mechanical behavior of the analytical model, because other calculations run for longer bodies indicate the agglomeration and moving away not only of the first "torn" group of vortices but a second group on the opposite side as well.

The comparison of predicted circulation distribution with that calculated from the wind tunnel flow field data is shown in figures 10a and 10b for BS 52 and 69, respectively. At the upstream station (fig. 10a), the predicted vorticity distribution tends to be centered farther from the body than the measured values. In particular, there is a strong

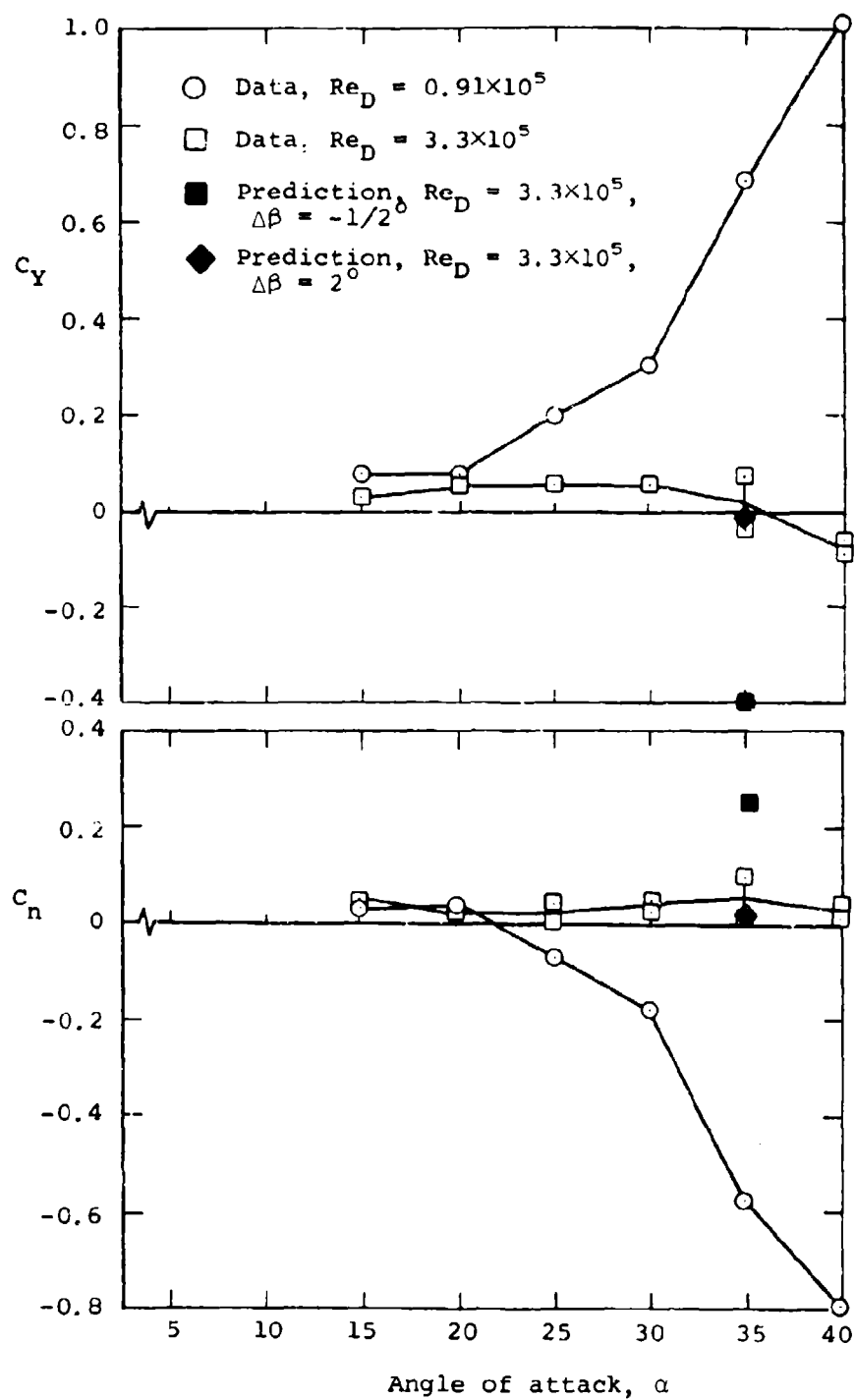


Figure 8. Side force and yawing moment for V/STOL nose alone at $\beta = 0$.

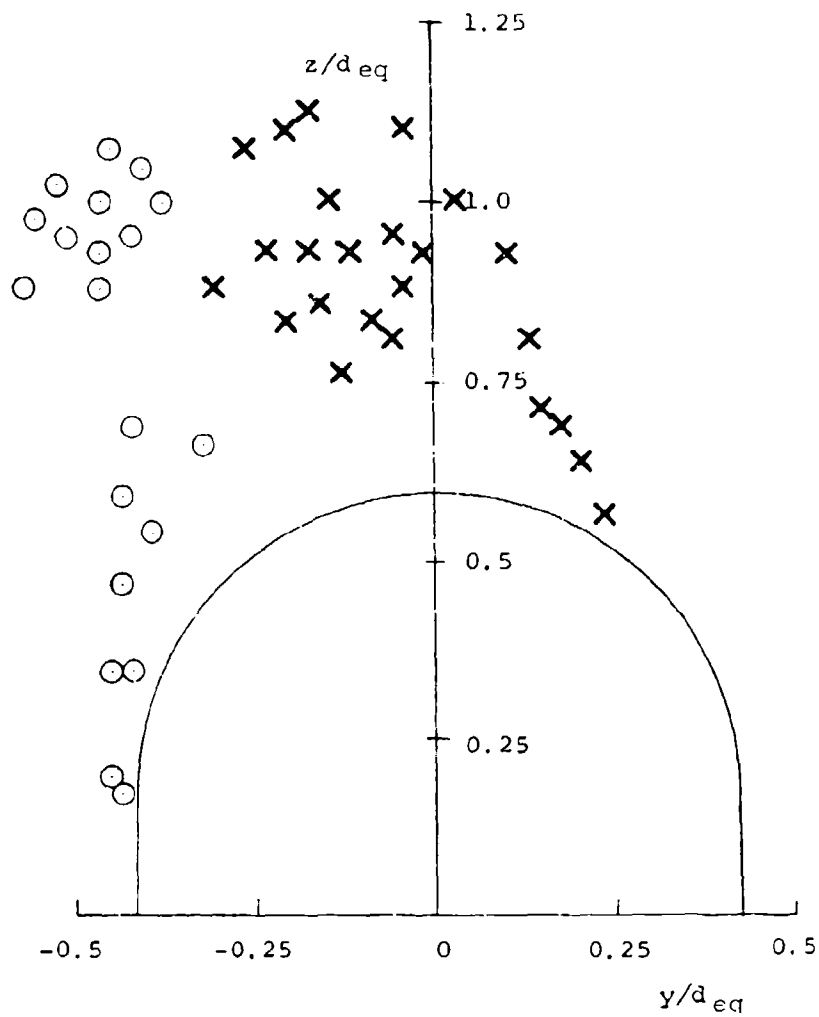
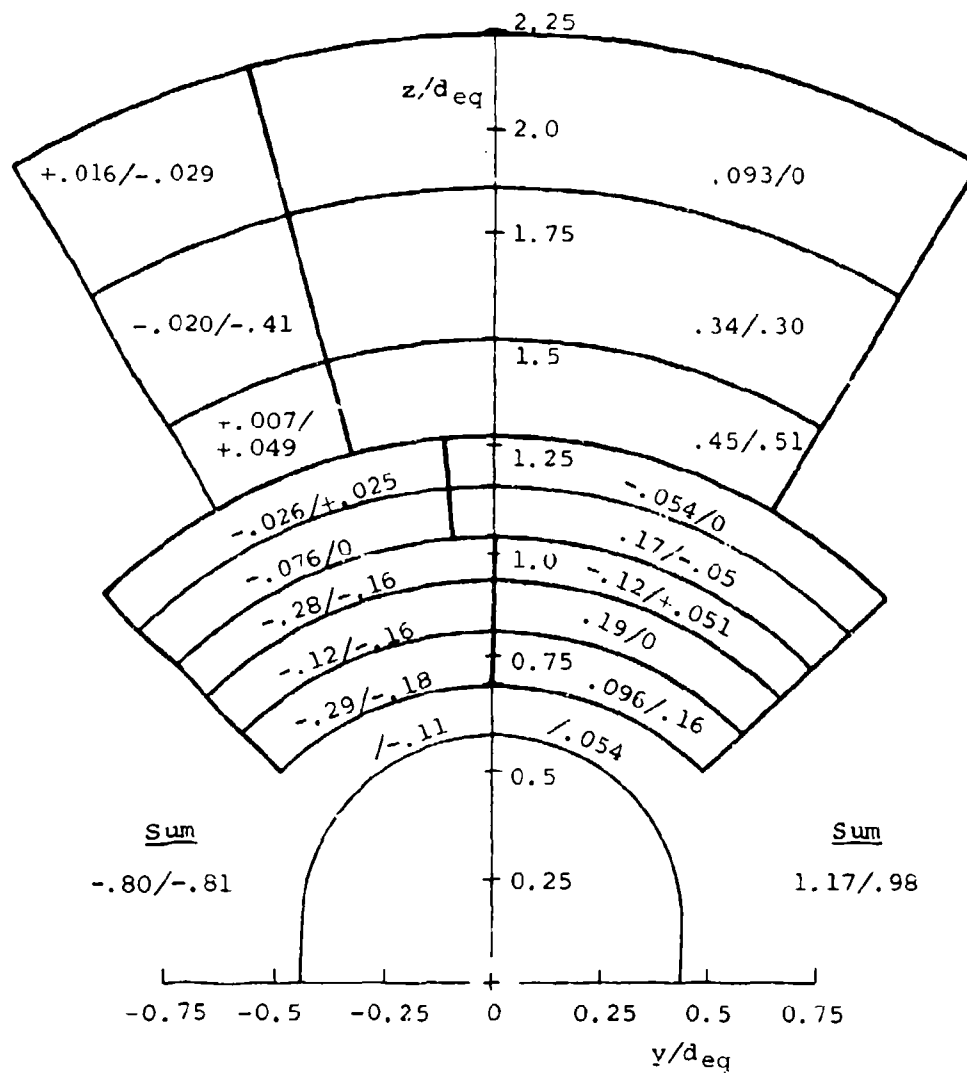


Figure 9. Predicted vortex cloud positions for V/STOL body at BS 52 for $\alpha = 35^\circ$, $\beta = 10^\circ$.



(b) BS 69.

Figure 10. Concluded.

area of predicted vorticity associated with the upper left group of vortices in figure 9, which does not show in the data. The predicted net positive and negative circulation values do not show as much difference as the measured values.

The boundary between the positive and negative circulation areas has an influence on these comparisons. The boundary was selected in the following manner. Because of the large number of data points included within the region through which the rake was moved, it is possible to form small sectors consisting of four adjacent data points, calculate a circulation for each small sector, and plot these circulation values against angular position of the rake. Typically, these plots will show a variation from positive values on the right to negative values on the left, and the angular boundaries in figure 10 were selected as those locations where the sign of the local circulation changed. One can see from the predicted distribution of figure 9 that the boundary of figure 10a passes through the cloud of positive vortices over the top of the body. Thus some of the positive vortices are included in the negative vorticity side, which tends to reduce the predicted magnitudes of both the positive and negative circulations, both in the individual regions and the total. While this effect would improve the comparisons in the regions near the body, it does not account for the large predicted negative circulations away from the body.

For the downstream station (fig. 10b), the general form of the circulation distribution on the windward or right side is well predicted and shows both predicted and measured concentrations of circulation near the body that is shown by the theory, but as in the previous case there is a very large predicted circulation well above the body that does not appear in the data. At intermediate heights above the body on both right and left sides, both the predicted and measured values of circulation are low.

This is a case where the selection of the angular boundary between the positive and negative circulation regions has a considerable influence on the predicted distribution and the comparison with data. The same case was calculated with the boundaries between the right and left sides rotated five degrees to the right for all regions. The measured distribution does not change a great deal with the boundary change, although the values of negative circulation on the right and positive

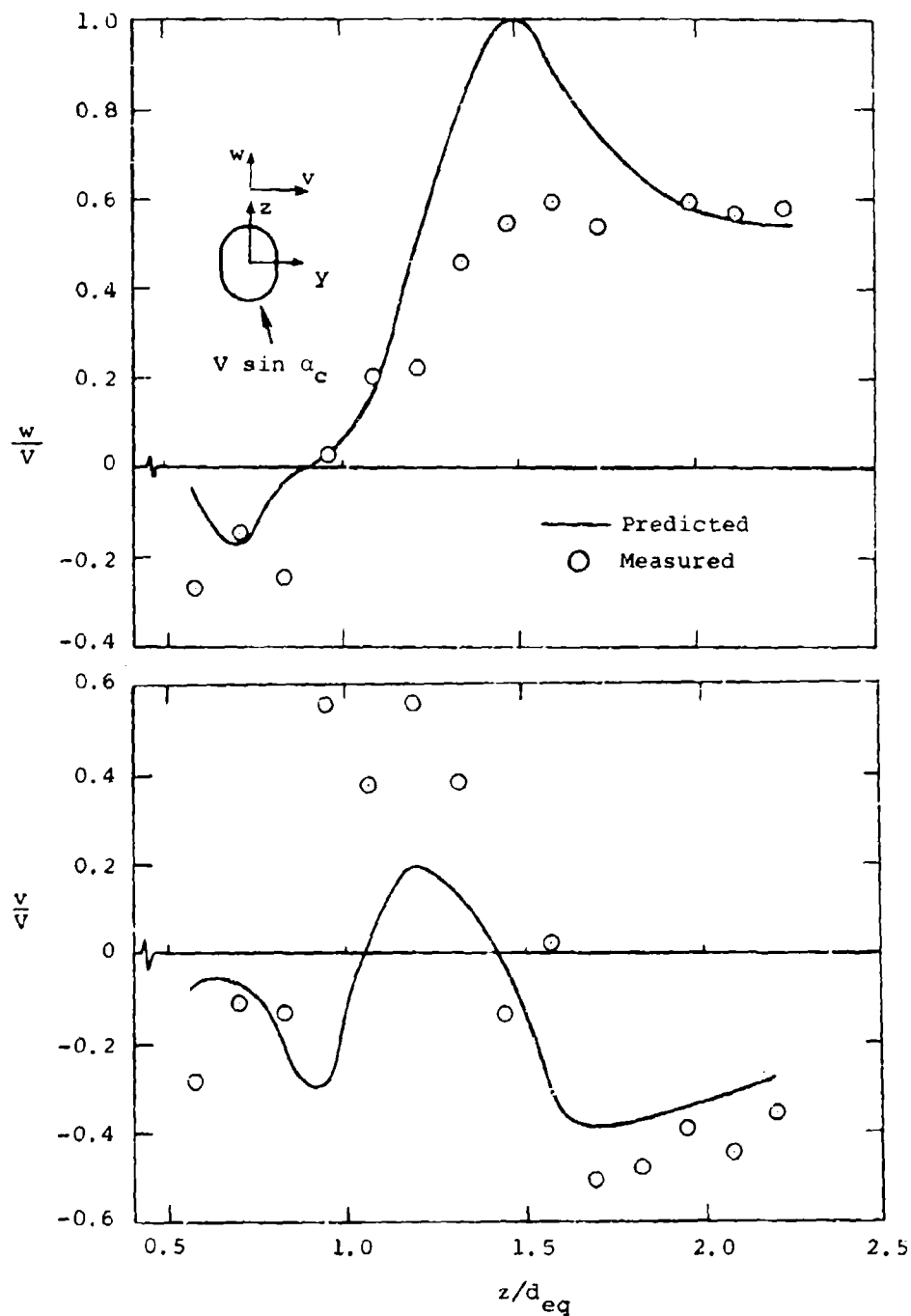
circulation on the left become smaller. However, in the prediction there are many positive vortices along the boundary between the right and left sides, and with the small change in boundary, about one-third of the positive vorticity is changed from right to left regions, greatly reducing both the net positive and negative circulations.

A comparison of induced velocities in the flow above the body is shown in figures 11a and 11b. Figure 11a shows the u/V and w/V velocity components along a line above the body in the plane of body symmetry ($\theta = 90^\circ$), and figure 11b shows similar results along a radial line 18° to leeward of the plane of symmetry ($\theta = 108^\circ$). As in the zero sideslip case, the predicted velocities show the same form as the measured values in three of the four cases. For the upwash velocity, w/V , at $\theta = 108^\circ$, there is a region of large discrepancy at about two diameters, which corresponds to the large predicted area of vorticity noted in figure 10b which was not seen in the data.

These results are typical of a large number of flow field comparisons made. The agreement is not consistent and is good in some cases and unsatisfactory in other cases. The data show a progression from a pair of relatively concentrated vortices at the upstream station (BS 52) to a rather complex vorticity distribution at the downstream station (BS 69). In a qualitative way, the water-tunnel flow visualization results confirm the wind tunnel measurements, in that no well defined core was visible with this nose shape, unlike the results with the F-5 nose. It would be desirable to have flow field data on a noncircular shape exhibiting the more concentrated vortex system of the F-5 to evaluate the method further.

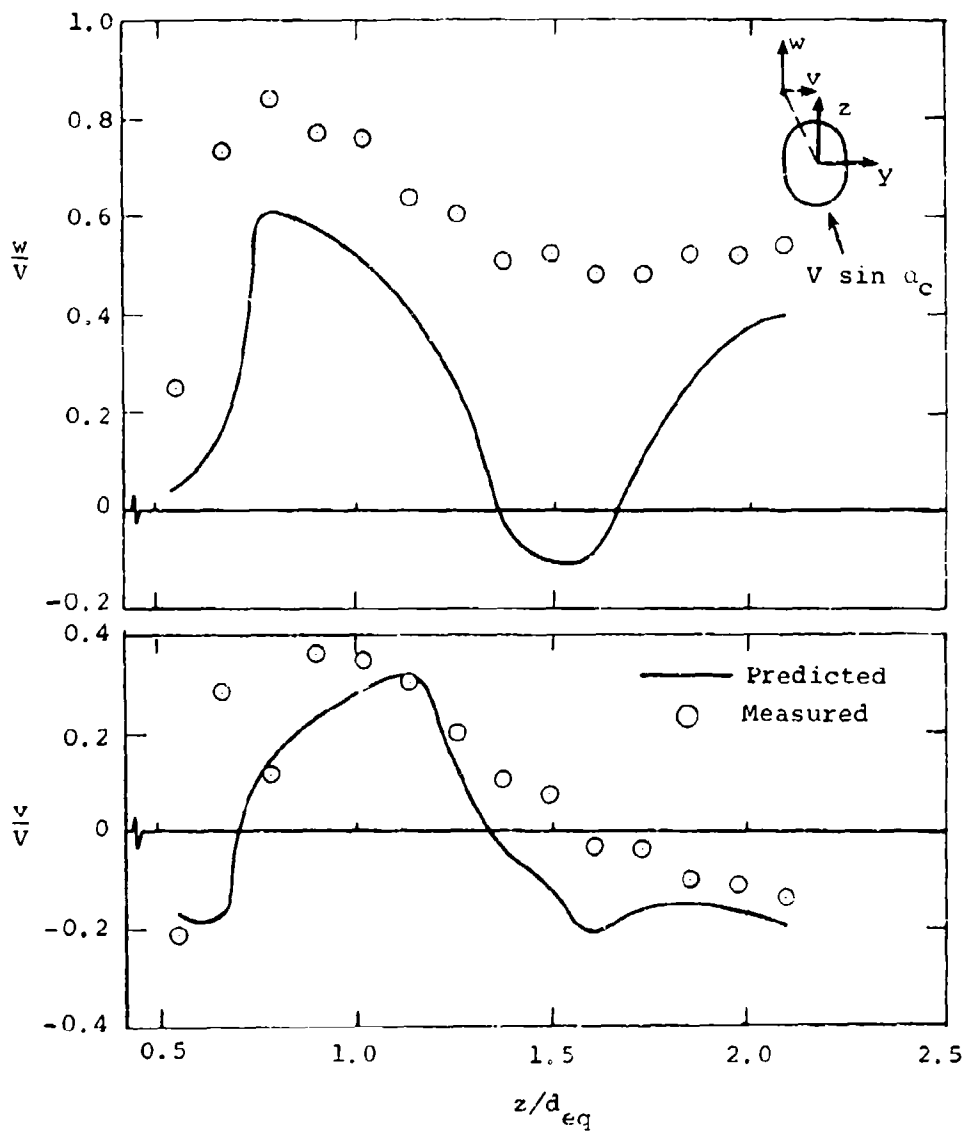
The comparison of predicted and measured side-force and yawing-moment coefficients is shown in figure 12. The data are from the water tunnel tests at Nielsen Engineering & Research. There is a large Reynolds number effect in the data that is probably associated with a change from subcritical to supercritical crossflow. The high Reynolds number case is more representative of the wind tunnel tests which were run at about twice the maximum Reynolds number available in the water tunnel. The predicted side-force and yawing-moment coefficients agree very well with the high Reynolds number data.

Some predicted results for the location of the two separation lines on the V/STOL nose at $\alpha = 35^\circ$ and $\beta = 10^\circ$ are shown in figure 13. Two



(a) In vertical plane of symmetry.

Figure 11. Predicted and measured crossflow plane velocities above V/STOL body at $\alpha = 35^\circ$, $\beta = 10^\circ$, BS 52.



(b) Along a line 18° off the vertical plane of symmetry

Figure 11. Concluded.

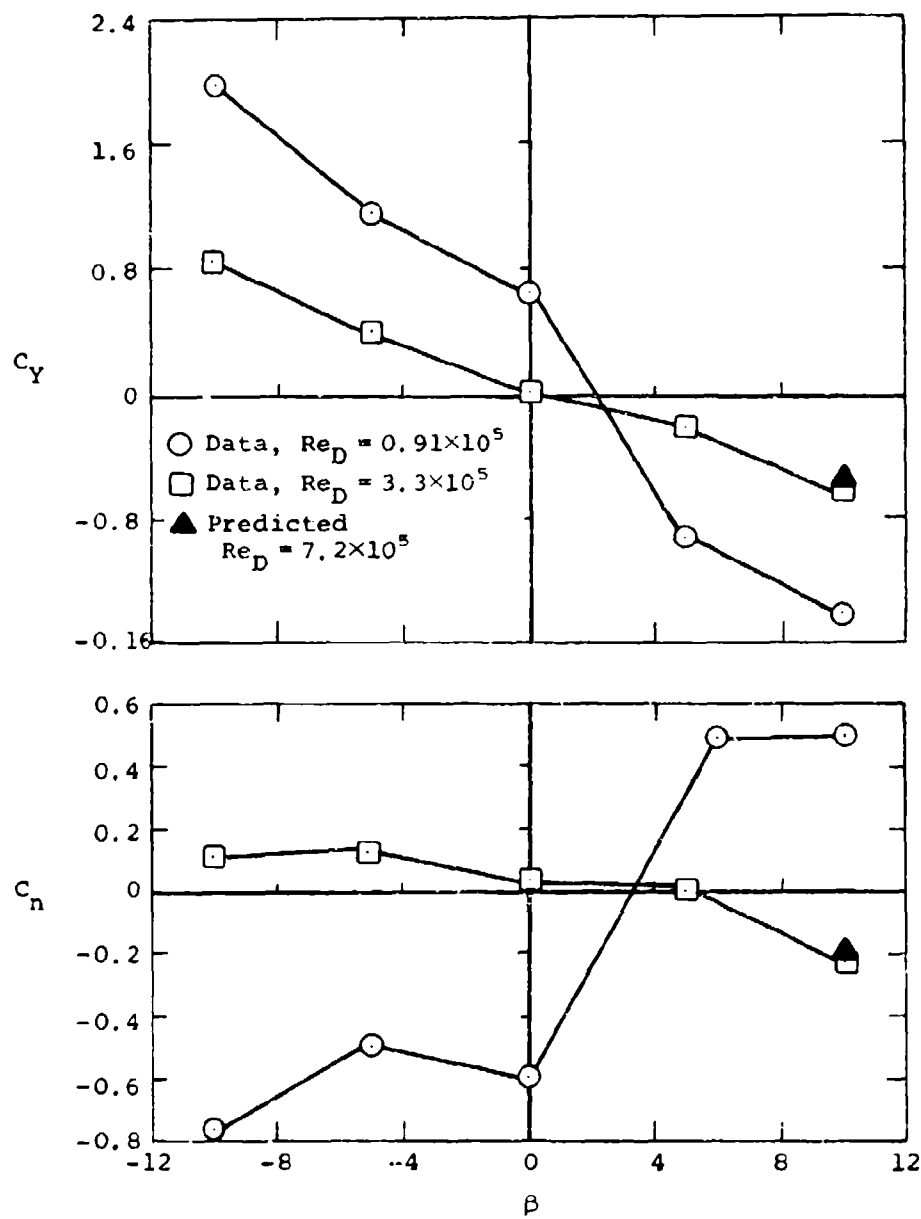


Figure 12. Predicted and measured side force and yawing-moment coefficients on V/STOL nose at $\alpha = 35^\circ$.

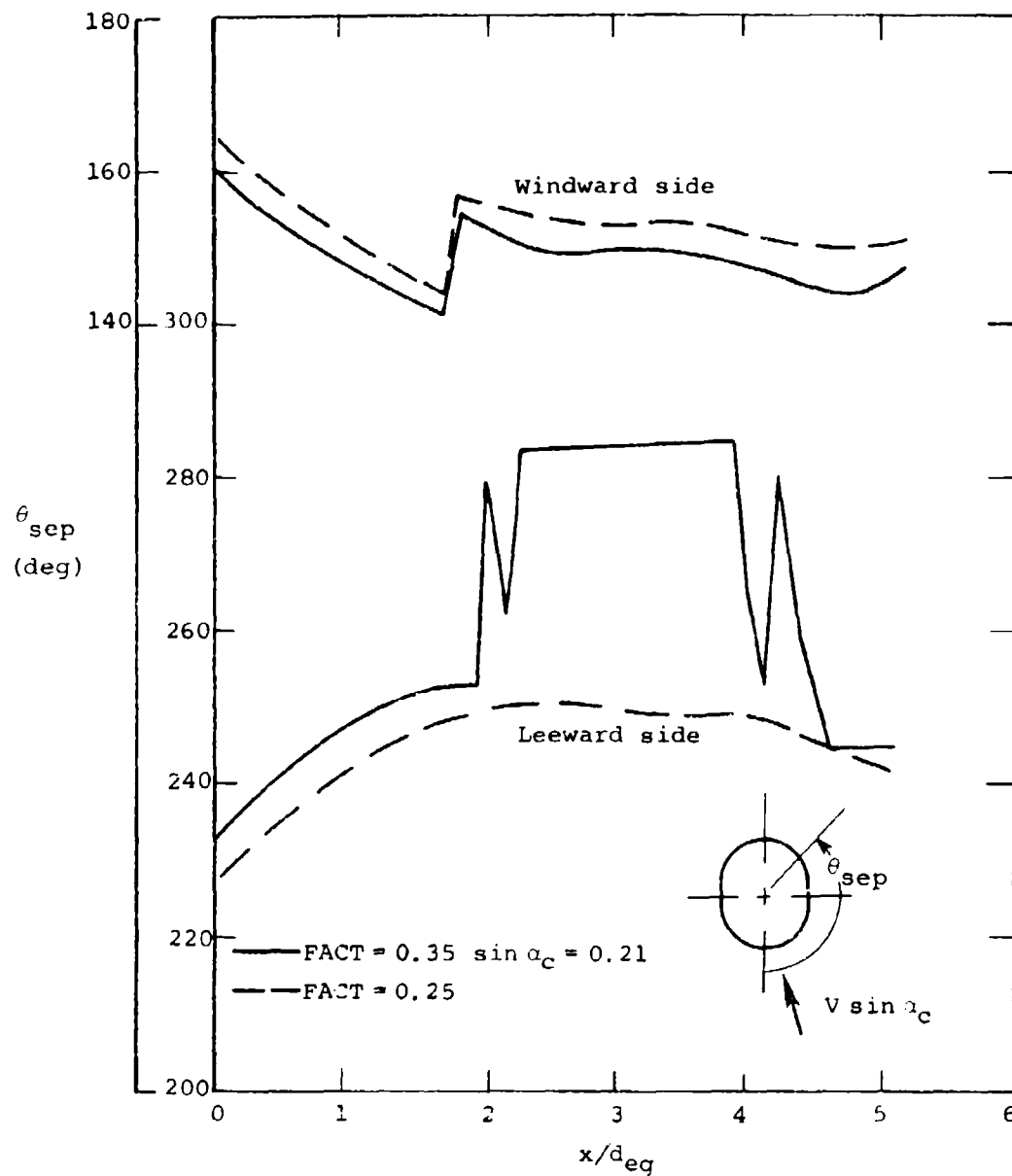


Figure 13. Predicted separation location on V/STOL nose at $\alpha = 35^\circ$, $\beta = 10^\circ$ for two separation criteria.

sets of results are shown for two different separation criteria. The first is the modified Stratford criteria, $0.35 \sin \alpha_c$, which was found to give good results in comparison with measurements on circular cross-section ogive-cylinders at low speeds. For this case, the resultant factor is 0.21. The second criterion used is a value of 0.25, which was chosen to provide a somewhat longer run length before separation than the 0.21 value gives.

Over the forward part of the body (the first two diameters of length), the two sets of separation angles are very similar in shape and are about 5 degrees apart. On most of this part of the body, the cross section is circular or near-circular. Further aft, on the part of the body which has flat sides, the two sets of results still look similar on the right hand or windward side. In this case, separation occurs at the top of the flat side where the flow first encounters an adverse pressure gradient.

On the left or leeward side, the flow must travel a longer distance to reach the flat side. With the modified Stratford criterion and the very small pressure gradients on the flat surface, the predicted separation point was found to jump between 250° and 290° across the flat surface as distance along the body changed. The jumps in separation point cause the vortices to be introduced into the flow at different locations, which influences the motion of the vortices and, more importantly, influences the surface pressure distribution and separation at the next axial station. When the criterion was changed to 0.25 to provide a slightly longer run length, the predicted separation point was stabilized at the upper end of the flat surface ($\theta = 250^\circ$). There are no separation data available to provide guidance to the theory on the accuracy with which the separation line location is predicted, and such a verification would be very desirable, both for bodies which have relatively flat surfaces with low pressure gradients and for curved surfaces.

5.1.2 F-5 configuration.- The data available for this nose configuration consist of water tunnel forces and moments and vortex locations and wind tunnel forces and moments, all at comparable Reynolds numbers. The Langley Research Center nose model has a length of 32 percent of the fuselage, which includes a short portion of the canopy, whereas the NEAR model has a length of 41 percent of the fuselage, which is the length back to the intersection of the strake leading edge with

the fuselage. For purposes of applying the nose separation flow model, the inflection in curvature of the cross section shape where the canopy joins the fuselage could not be modeled accurately by the numerical mapping and this region was smoothed to permit the mapping analysis to work properly.

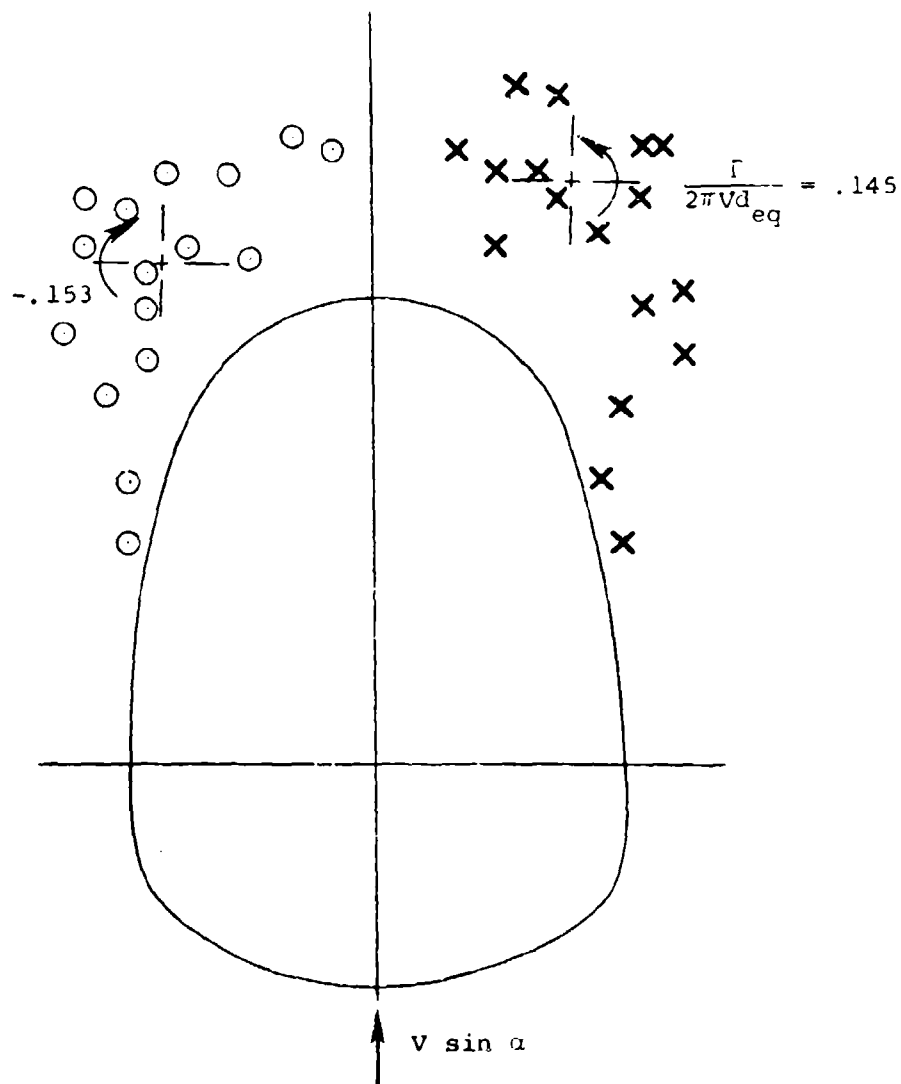
The flow conditions examined were $\alpha = 30^\circ$ and 40° and $\beta = 0^\circ$ and 10° . For the zero sideslip case, an asymmetric disturbance to the calculation of 1/2-degree rotation of the separation points over the first 10 percent of the nose length was used, as in the V/STOL model.

Predicted vortex cloud distributions are shown for a number of cases in figure 14. In the cases with sideslip, the calculations were made with a negative sideslip for convenience, but a positive sideslip would merely reverse the two sides of the vortex pattern. All cases except figure 14c show the vortex positions at the 41 percent body station corresponding to the length of the water tunnel model. That figure shows the vortex positions at the 32 percent body station. In some cases, the computer program will combine two vortices, if they are very close together, into a single vortex having the strength of the two and a position which is the "center of gravity" of the two. In these cases, the number of vortices shown in figure 14 may not be the same on the right and left sides, although an equal number are shed.

For $\alpha = 30^\circ$ and zero sideslip (fig. 14a), the vortex cloud shows an appreciable asymmetry which increases substantially at $\alpha = 40^\circ$ (fig. 14b). A comparison of vortex clouds between the 32 and 41 percent stations for the $\alpha = 40^\circ$ case is shown in figures 14b and 14c. There is a considerable increase in asymmetry between these two stations. For zero sideslip, the total vorticity on the right and left sides differ by less than 3 percent, with the vortex group closest to the body having the higher strength.

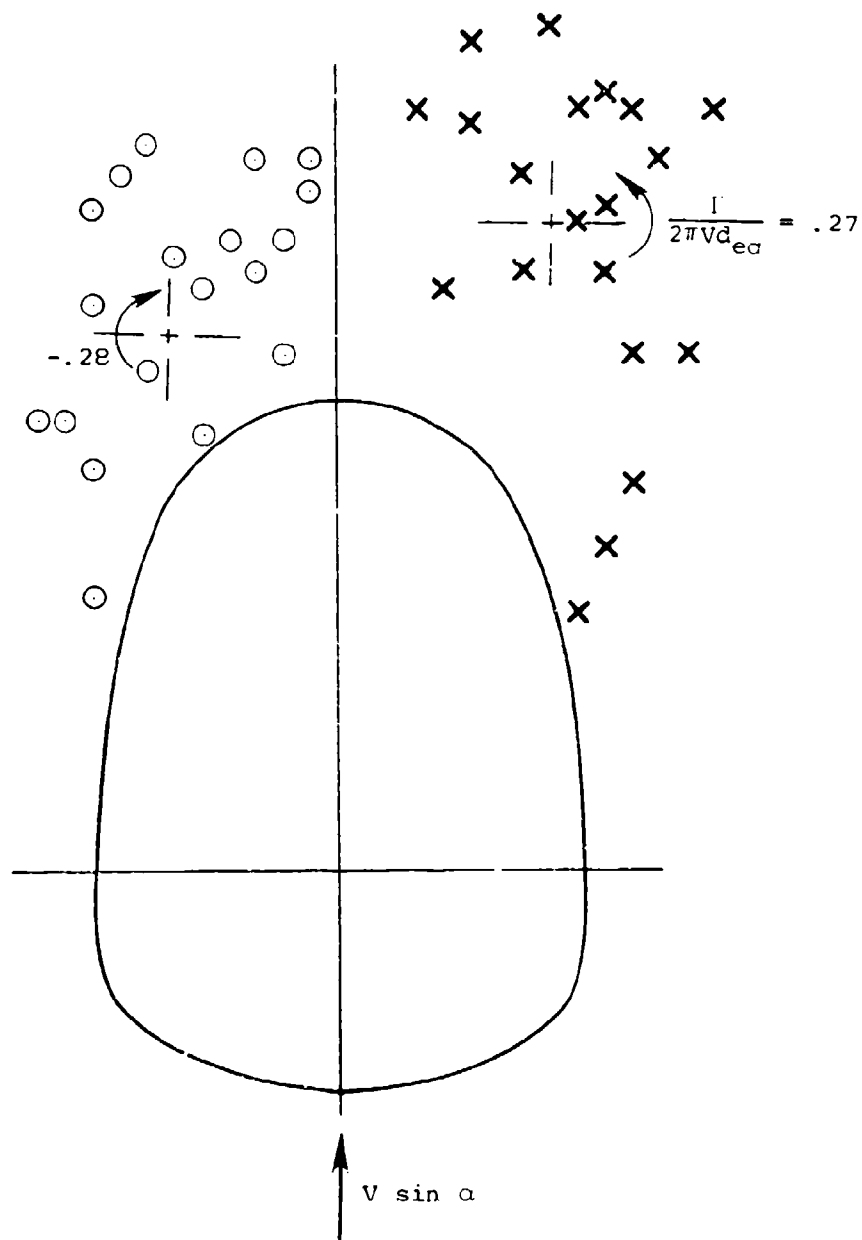
At ten degrees sideslip, the sidewash forces the windward vortex over the top of the body and the leeward vortex away from the body. The sums of the strengths of the right and left vortices are not as close in this case (within 10 percent), with the windward side being higher at 40 degrees angle of attack and the leeward side slightly higher at 30 degrees angle of attack.

The predicted vortex clouds are somewhat more concentrated for the F-5 than for the V/STOL nose, particularly at sideslip, and somewhat



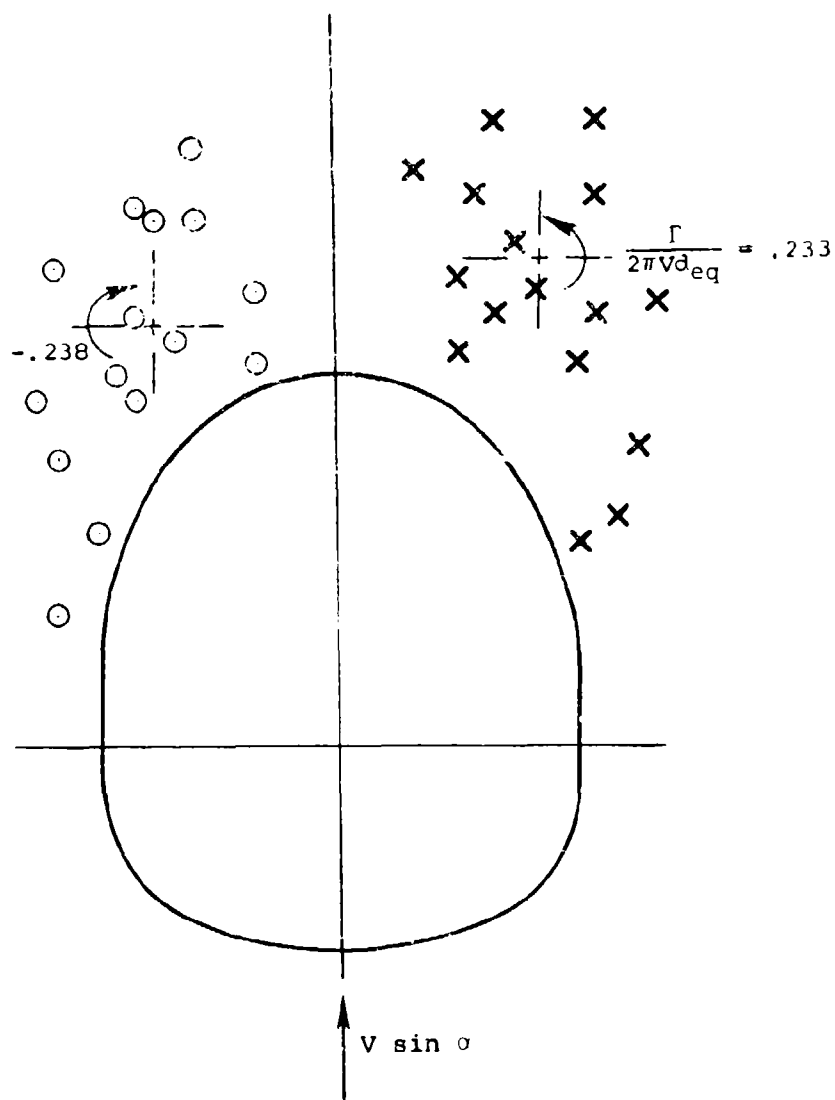
(a) $\alpha = 30^\circ$, $\beta = 0^\circ$, 41-percent station.

Figure 14. Predicted vortex cloud positions for F-5 nose.



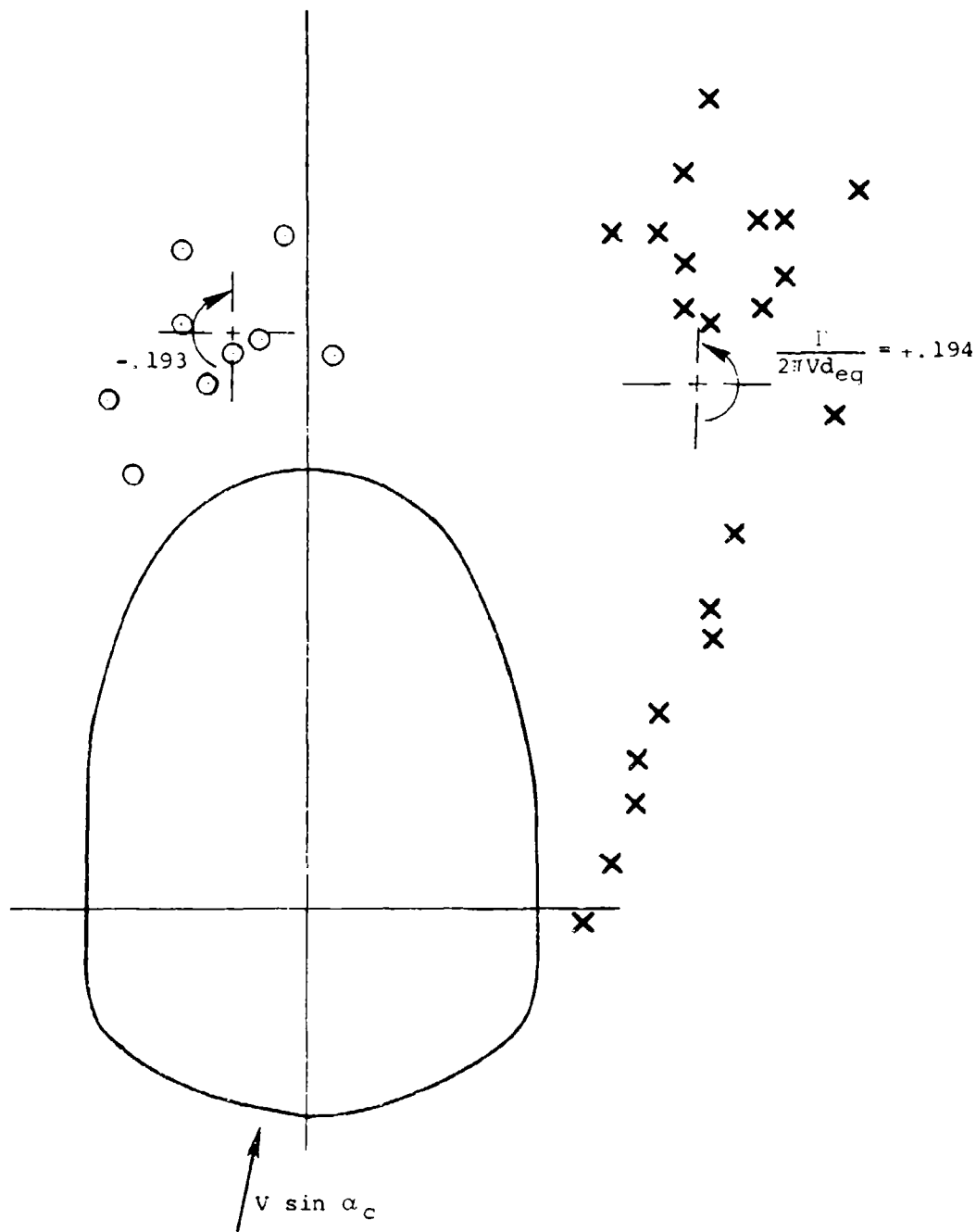
(b) $\alpha = 40^\circ$, $\beta = 0^\circ$, 41-percent station.

Figure 14. Continued.



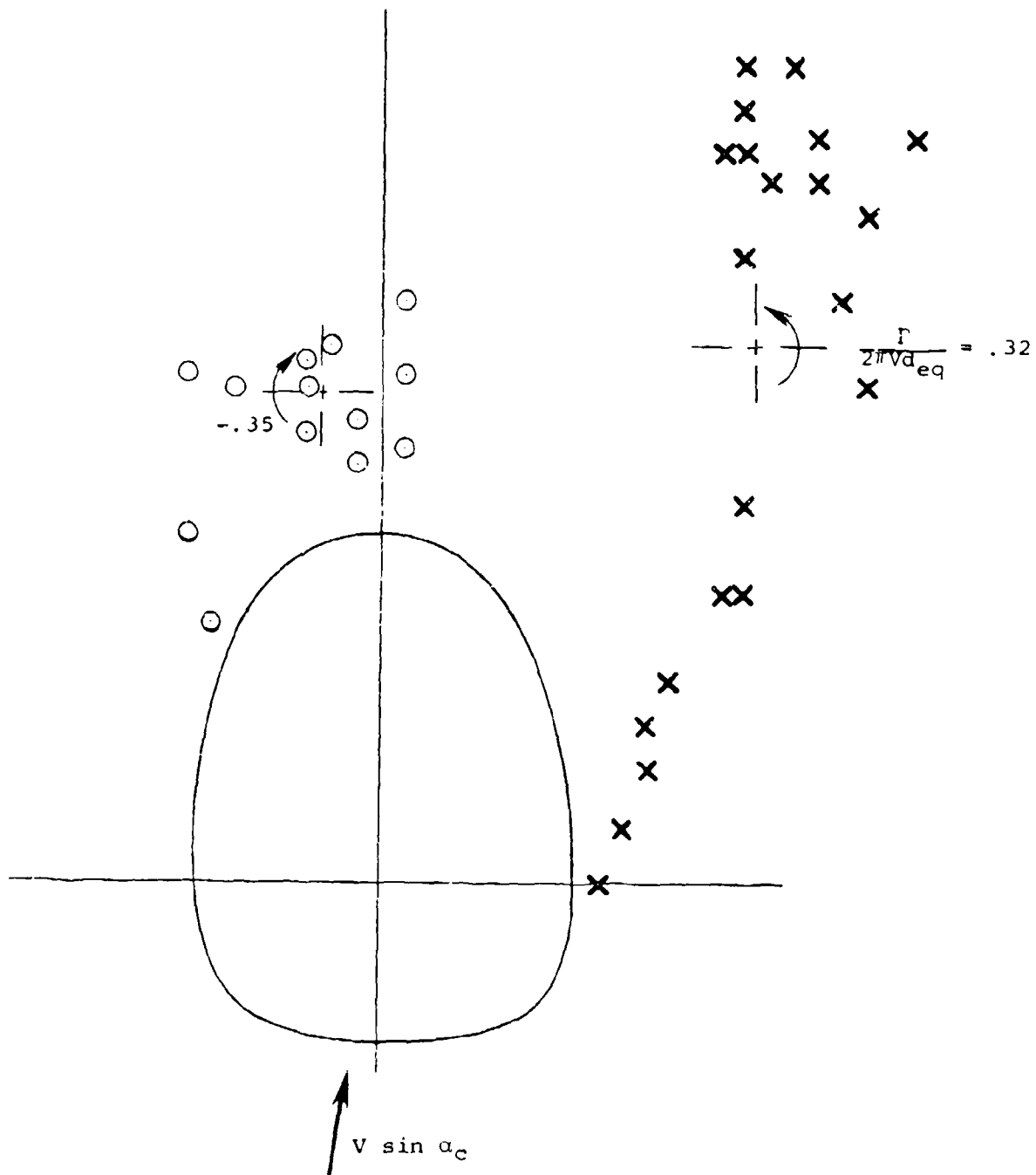
(c) $\alpha = 40^\circ$, $\beta = 0^\circ$, 32-percent station.

Figure 14. Continued.



(d) $\alpha = 30^\circ$, $\beta = -10^\circ$, 41-percent station.

Figure 14. Continued.



(e) $\alpha = 40^\circ$, $\beta = -10^\circ$, 41-percent station.

Figure 14. Concluded.

further from the body. This tends to agree with the qualitative observations of the flow visualization experiment in the water tunnel, which showed well defined cores for the F-5 nose and a more diffuse structure for the V/STOL nose (figs. 5 and 6 of ref. 3).

A comparison of predicted centers of vorticity with core locations determined from water tunnel tests is shown in figure 15. The core locations were obtained from air bubble photographs which showed rather clear, small, well-defined cores. The accuracy of core location measurement is about $\pm 0.05 d_{eq}$. The predicted centers include all vortices in the cloud on each side, some of which might be interpreted to consist of the feeding sheet rather than rolled up vorticity (for example the right side in fig. 14e). For clarity of presentation, all coordinates are considered positive and the curves for the right and left hand vortices are separated. In the case of nonzero sideslip, the right hand vortices are the windward vortices. For zero sideslip (figs. 15a and 15b) the heights of the vortices above the body are generally under-predicted while the predicted lateral positions of the vortex cores are in reasonable agreement. If the "feeding sheet" vortices were left out of the center of vorticity calculation, the predicted heights of the centers would be higher and in better agreement with the measured values. For the case of 10 degrees sideslip (figs. 15c and 15d), the agreement as presented is quite good, and the foregoing feeding sheet consideration would not necessarily improve the agreement.

Comparison between theory and experiment for side-force and yawing-moment coefficients are shown in figures 16 and 17 for the 41-percent body length and 32-percent body length models, respectively. The longer model data are the NEAR water tunnel data and the shorter model data are from the NASA tests. Values are presented only at 30 and 40 degrees angle of attack. In the case of the water tunnel results, data are available at two Reynolds numbers, whereas the calculations were made only for the lower Reynolds number.

Figure 16 shows for zero sideslip only small measured values of force and moment at both 30 and 40 degrees. The predicted loads at 30 degrees are small and agree well, but at 40 degrees the predicted loads are considerably higher than the data. The degree of asymmetry in the predicted vortex system is too large in this case.

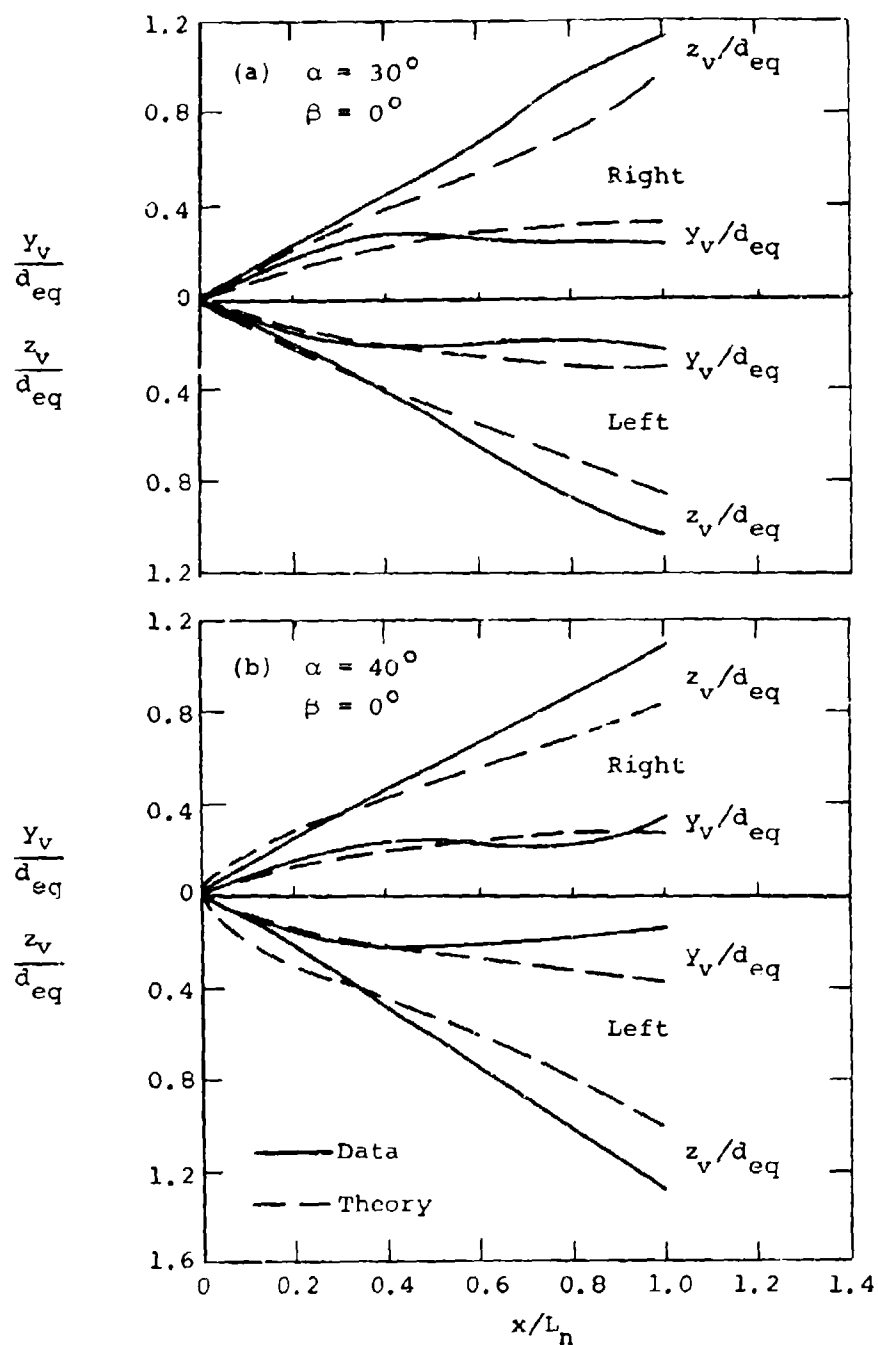


Figure 15. Comparison of measured and predicted vortex positions for F-5 nose.

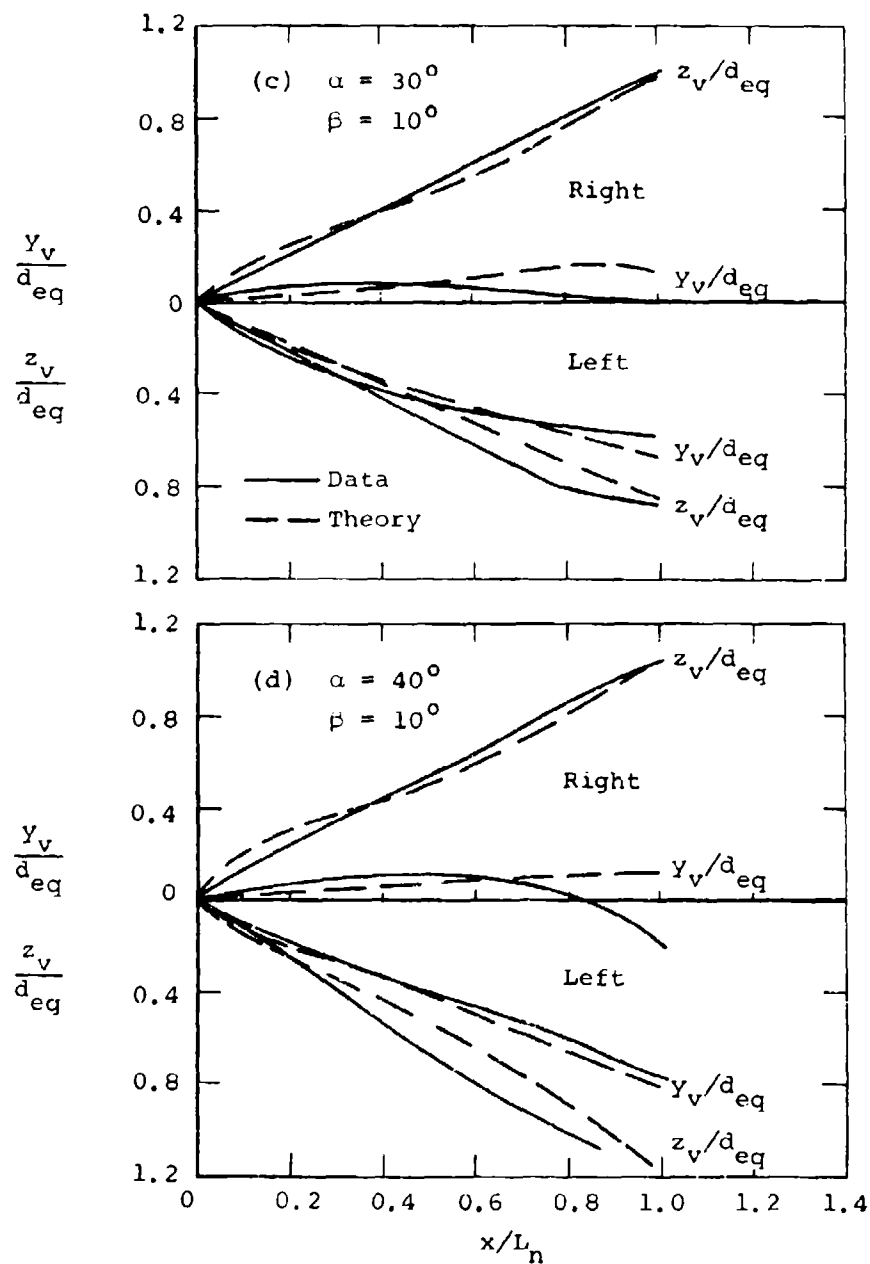


Figure 15. Concluded.

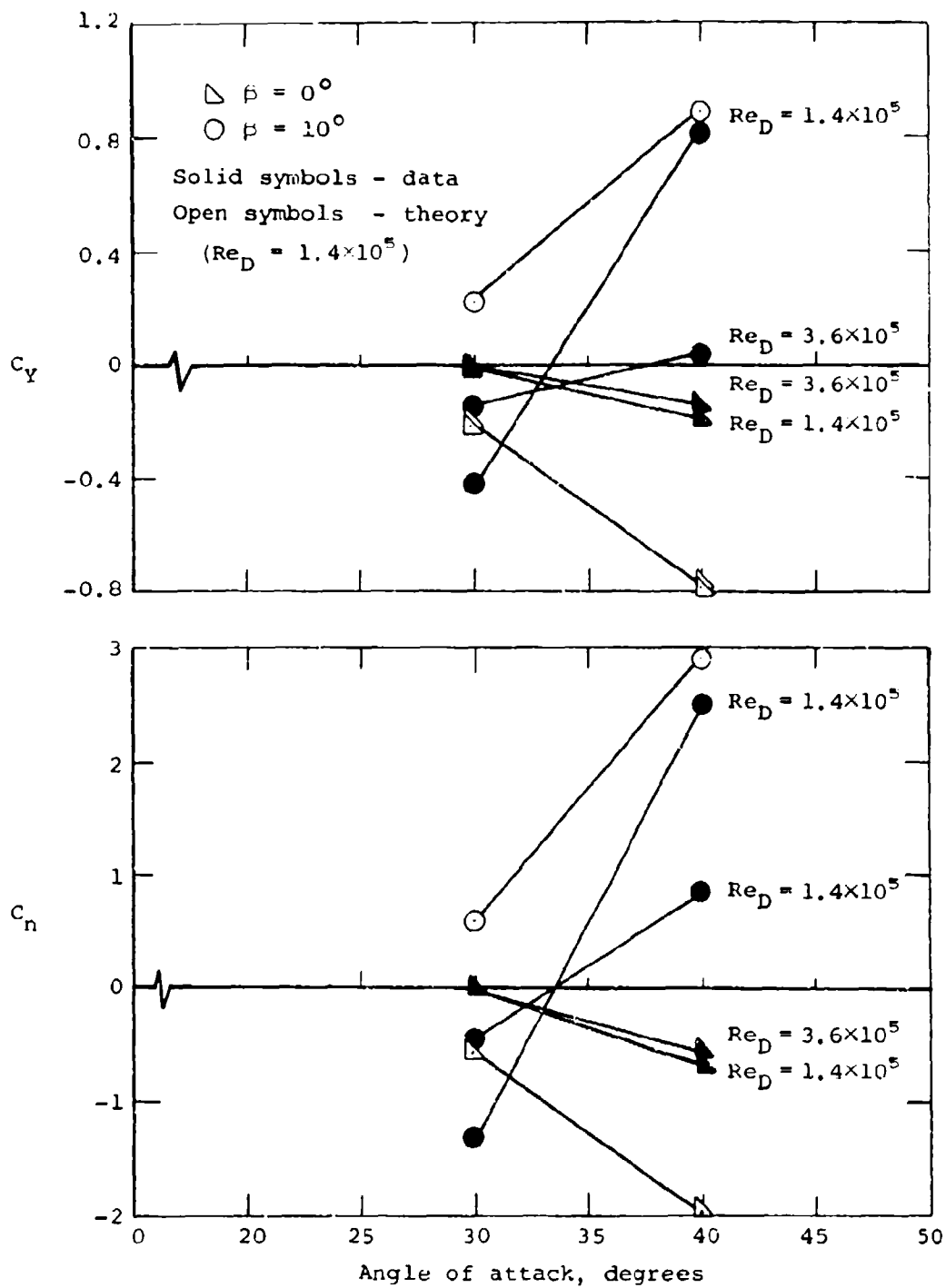


Figure 16. Comparison of side force and yawing moment water tunnel data and theory for 41-percent length F-5 nose.

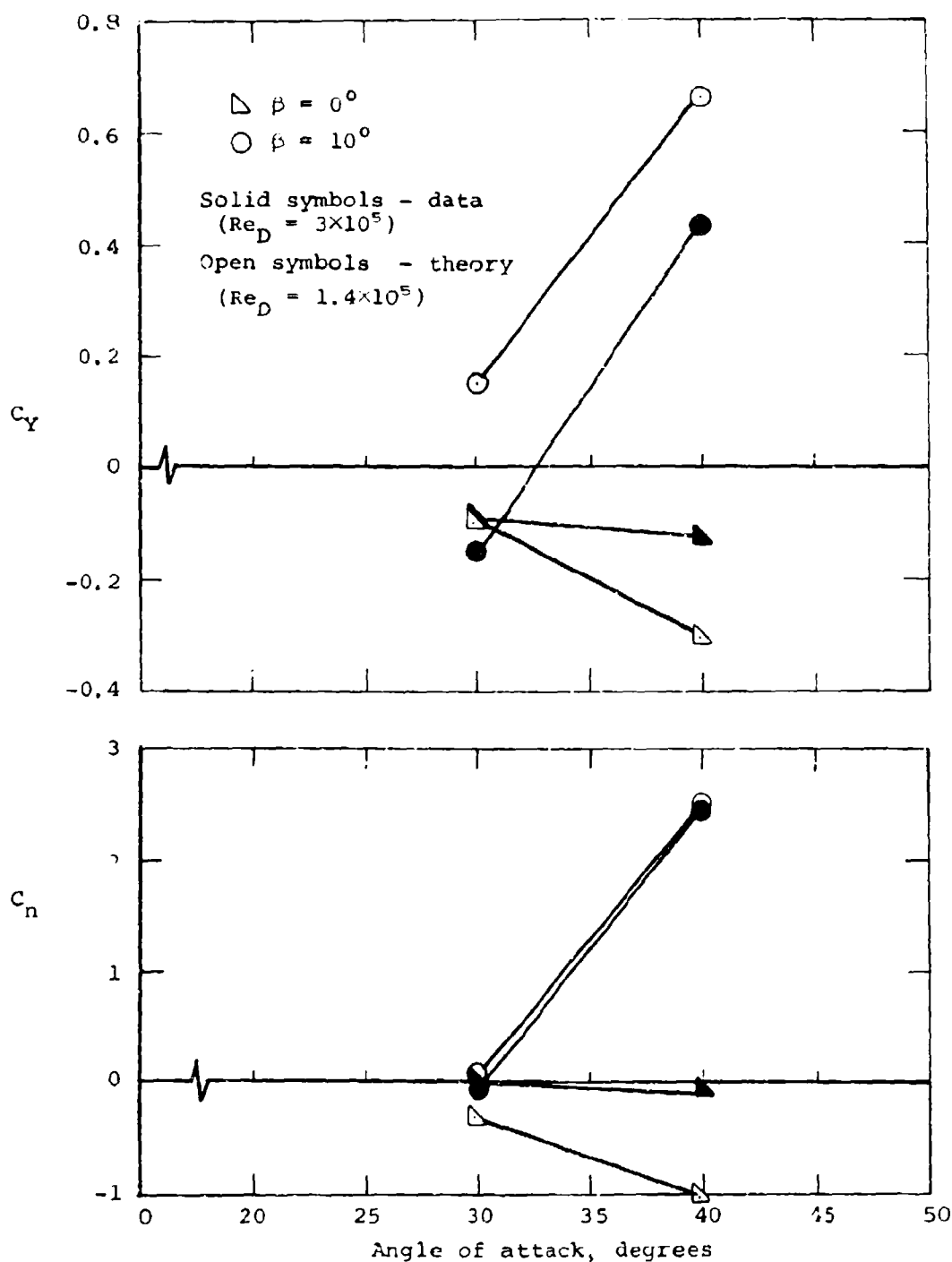


Figure 17. Comparison of side force and yawing moment wind tunnel data and theory for 32-percent length F-5 nose.

At 10 degrees sideslip, the data show a destabilizing yawing moment at 30 degrees and a stabilizing moment at 40 degrees for both Reynolds numbers, with a considerable effect of Reynolds number on the results. The theory shows good agreement with the low Reynolds number data at 40 degrees, but too high (too stabilizing) a load at 30 degrees. In the absence of separation, the predicted loads are negative (destabilizing) at both angles of attack, and the predicted influence of separation is to cause a stabilizing force, as is shown by the data, but of too large a magnitude.

For the shorter NASA nose model (fig. 17), the same trends are evident. The wind tunnel and water tunnel data are consistent in showing the reversal of sign of side force between 30 and 40 degrees angle of attack. At 10 degrees sideslip, the predicted and measured yawing moments are in better agreement than is the case for the longer model.

5.2 Complete Configuration

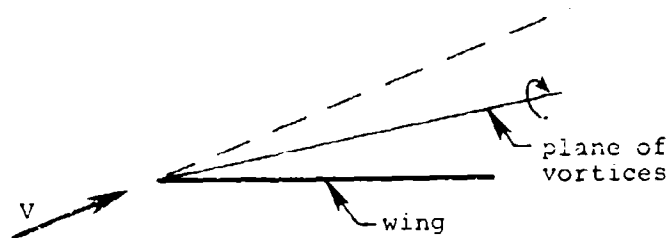
In applying the wing, body, and tail methods to a complete configuration, several decisions have to be made regarding use of the method. These are discussed first and are followed by presentation of results.

As an input to the wing/body calculation, the nose vortex system must be specified. Typically there are some 60 to 80 vortices in the cloud representing the distributed vorticity at the aft end of the nose. In order to limit computation time, the vortex chasing routine that determines the positions of the free vortices passing over the wing/body and the velocities induced on the wing/body is limited to 12 vortices made up of nose, strake and wing vortices. Thus the nose vortex cloud had to be represented by only a few vortices, and in practice between 2 and 6 vortices were used. Some calculations were made with two different fits to a given nose vortex system to determine sensitivity to the way in which the nose cloud was represented. These results are discussed below.

The calculation of wing/body loads uses the vortex lift concept (ref. 11) to account for leading edge separation. In the work of reference 8, it was found that the amount of suction that was rotated into the normal force direction was dependent on aspect ratio for delta wings, and this dependency was ascribed to leading edge sweep. Using the work

of reference 8 as a guide, the strakes on both the V/STOL and F-5 configurations have sufficient sweep that full vortex lift is produced. Full vortex lift was also assumed to occur at the wing tips, although the contribution is small. On the wing leading edges of both configurations, however, the sweep is sufficiently small that no vortex lift is predicted to occur, and none was assumed to exist on either the V/STOL or F-15 configurations.

The strake leading-edge separation vortices are specified in strength and lateral position by the vortex lift that they represent. The vertical position, however, is not defined and has been specified on the basis of known vortex locations on delta wings. These data show that the vortex above the leading edge follows a path that in height lies about half way between the plane of the wing and the free stream direction, as shown by the sketch. The wind tunnel data permit an evaluation of this assumption



for the V/STOL configuration, and results are presented on this evaluation.

For the V/STOL model without vertical tail and the F-5 model, a section of afterbody is present. The positions of the nose vortices (and strake vortices, if present) and wing trailing edge vortices are determined over the length of afterbody to determine vortex-induced loads on the afterbody. In the case of the F-5, the afterbody is considered to extend from the wing trailing edge aft to the leading edge of the mean aerodynamic chord of the vertical tail. For calculating tail loads, the vortex positions at the leading edge of the mean aerodynamic chord of the vertical tail are used with the tail vortex-interference model.

In the case of sideslip, the vertical tail produces a direct side force which must be added to the side force induced by the vortices. This direct side force was predicted using the results of reference 9, together with slender body factors for the influence of the body on tail force. In both configurations, vertical-tail-on and tail-off data are

available at low angles of attack and sideslip which verified the predicted direct side forces on the vertical tail.

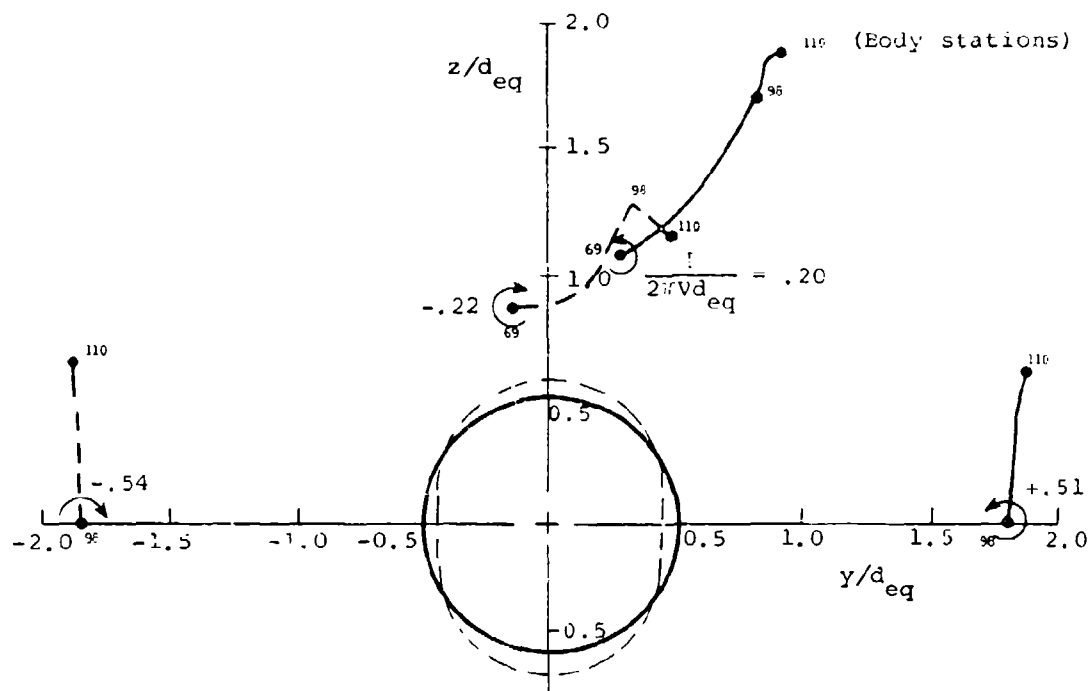
5.2.1 V/STOL model.- Consider first the results at zero sideslip and 35 degrees angle of attack. For the case of no strakes and no vertical tail, the nose vortex cloud at BS 69 was fit with both a two vortex and a six vortex model to determine the sensitivity of the results to the way in which the cloud is modeled. The results for vortex positions over the configuration downstream of the nose are shown in figures 18a and b for 2 and 6 nose vortices, respectively. These figures show the locus of vortex positions in successive crossflow planes, with several values of the body axial station noted on the vortex trajectories. The strengths of the vortices are noted at the initial axial station (BS 69). For purposes of calculating vortex positions, the body is assumed circular, and both the actual shape and the equivalent circular shape are shown.

For the six-vortex fit (fig. 18b), a more complicated interaction between nose vortices and the free stream occurs. The two upper vortices move generally upward with little lateral movement. The lower two positive vortices on the right side move towards the left. The lower two negative vortices move upwards, one rising to a high height above the body and the other rising much less and to the left. The "center of vorticity" of the positive and negative groups of vortices at the wing trailing-edge station are quite different than the positions of the two vortices of figure 18a. For the positive circulation group, the height is slightly greater, but the lateral position is to the left of the body symmetry plane rather than on the right side as in figure 18a. For the negative circulation group, the height is also slightly greater, but the center remains on the left side rather than on the right as in figure 18a. These differences result in a different sign of the vortex-induced side force coefficient on the wing/body portion of the configuration, which changes from $-.009$ for the two-vortex model to $+.004$ for the six vortex model. These differences are discussed further in a subsequent presentation on overall forces and moments.

A measured distribution of vorticity at the axial station of the wing trailing edge (BS 98) is shown in figure 19. These results show a high positive circulation about 3 diameters above the right side of the body and negative circulation closer to the body on both the right and

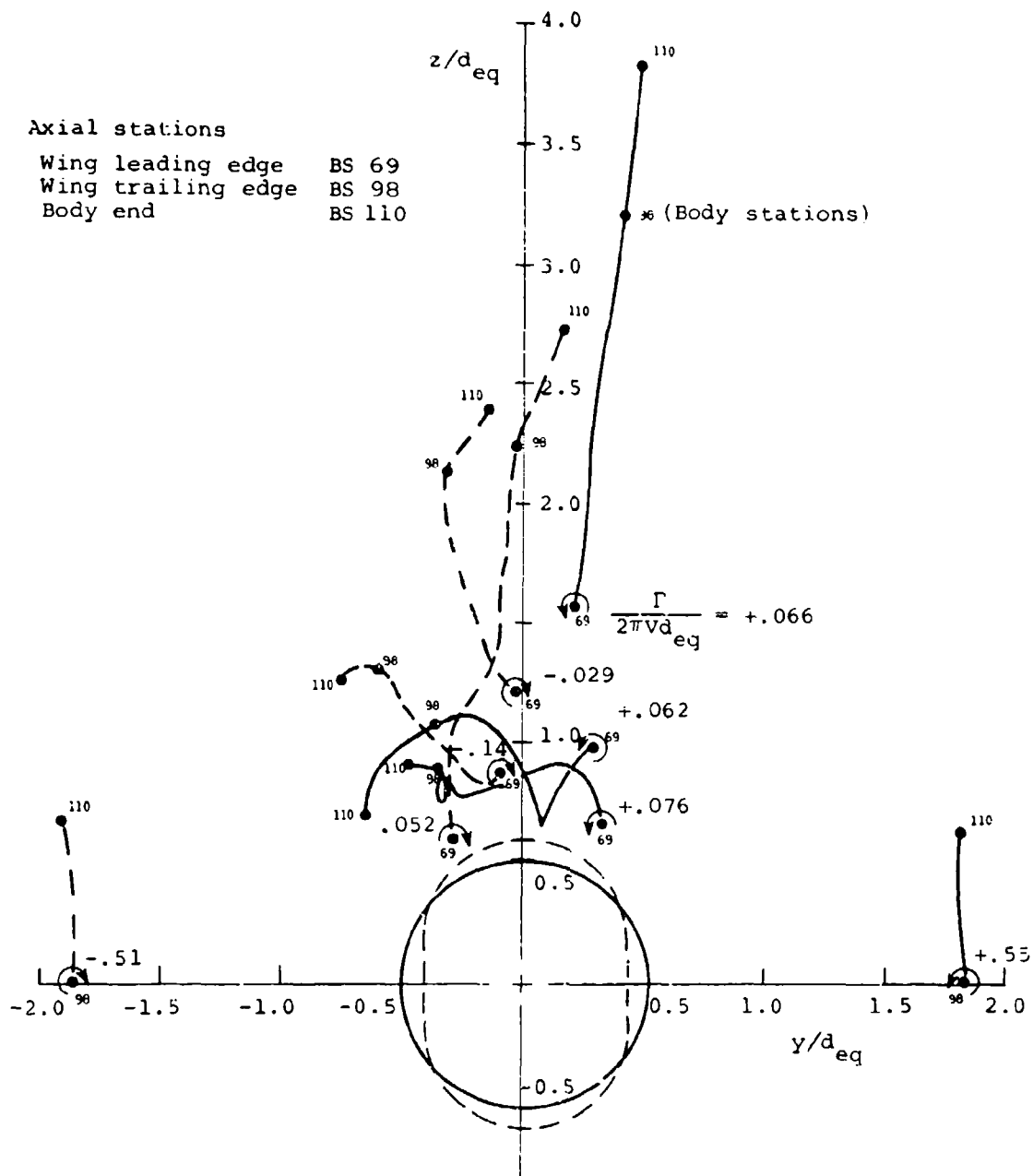
Axial stations

Wing leading edge	BS 69
Wing trailing edge	BS 98
Body end	BS 110



(a) Nose vortex cloud fitted with two vortices.

Figure 18. Predicted vortex positions over length of V/STOL model
for $\alpha = 35^\circ$, $\alpha = 0^\circ$, $\Delta p = -1/2^\circ$, no strakes.



(b) Nose vortex cloud fitted with six vortices.

Figure 18. Concluded.

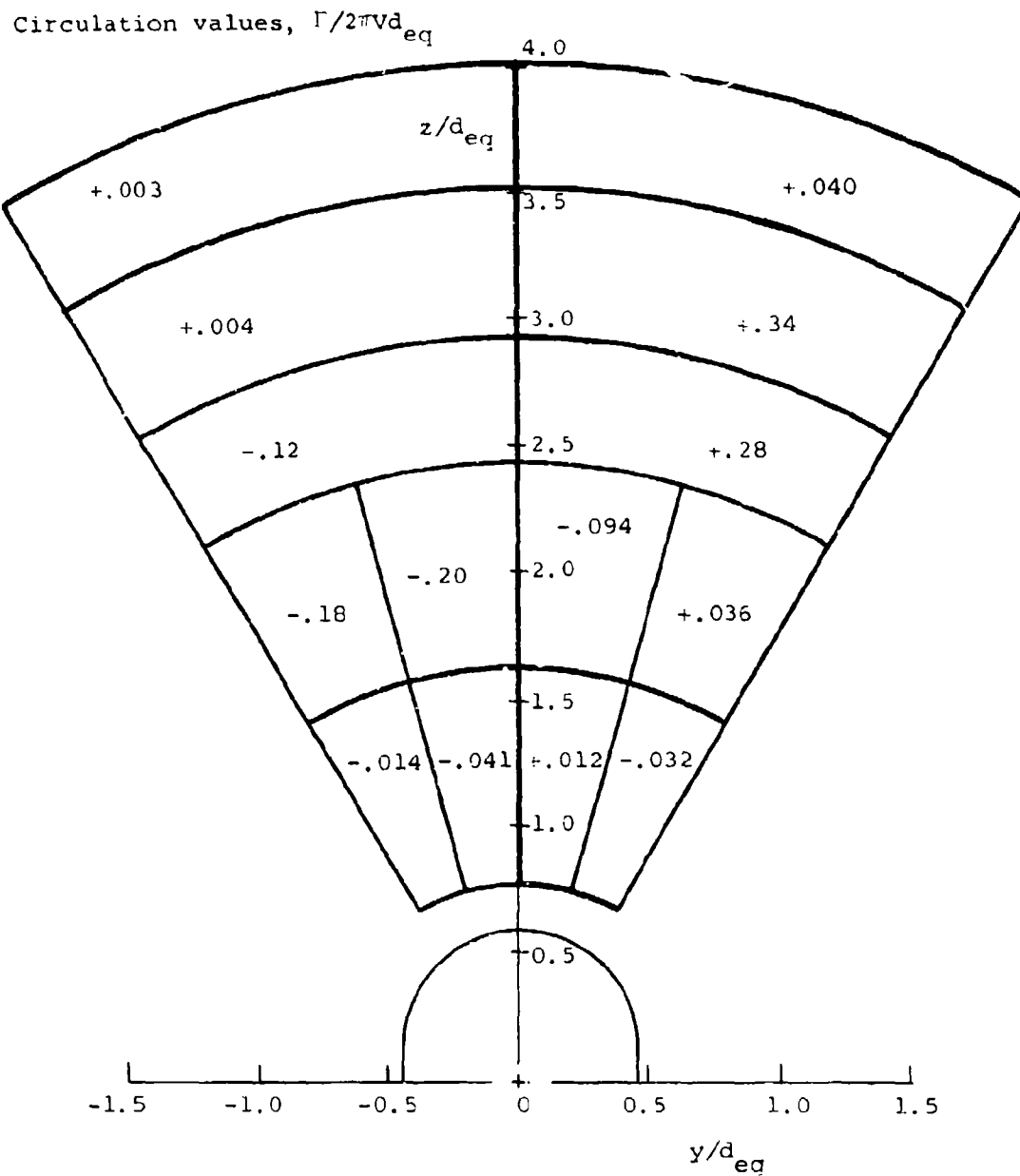


Figure 19. Measured circulation distribution over V/STOL body at wing trailing edge (BS 98) for $\alpha = 35^\circ$, $\beta = 0^\circ$, strakes off.

left sides of the vertical plane. While it is difficult to make comparisons between figures 18 and 19, it appears that the two-vortex model of figure 18a better fits the measured results than the six-vortex model of figure 18b.

The influence of initial strake vortex height is shown in figures 20a and 20b for the case of strakes on and vertical tail off and a two-vortex nose model. The two strake vortices originate as free vortices at the strake-wing intersection along the leading edge (BS 56) and generally move upward under the influence of the free stream. Figure 20a shows the resulting vortex motion for the case of the initial strake vortex height being given by delta wing data; that is, half way between the free stream direction and the wing surface. Figure 20b shows the same results for an initial vortex height half that given by the delta wing data. Also shown on these figures are measured strake vortex core positions as obtained from the flow field survey data.

The results of these two figures show that the predicted strake vortex position is higher than the measured value when started in accordance with delta wing results (fig. 20a), whereas a lower initial position results in better agreement. There is a considerable difference between the predicted paths of the nose vortices in these two cases, because the lower strake vortex positions cause more movement of the nose vortices. In the flow field data, the strake vorticity so dominates the flow that there is no apparent indication behind the wing of any nose vortex system, so no experimental evidence is available to evaluate nose vortex positions.

A series of comparisons of predicted and measured loads is given in Table I. The configurations considered are vertical tail on and off and strakes on and off. The "standard" case will be considered the nose vortex system that is produced with a 1/2-degree disturbance at the nose and represented by two concentrated vortices and a strake vortex system with an initial height given by the delta wing data. Compared with this case are predictions for cases in which one part of the calculation is changed. These include a nose vortex system produced by a 2-degree disturbance midway along the body, a strake vortex system with an initial height half that given by delta wing data, and finally a nose vortex system represented by six rather than two concentrated vortices.

TABLE I.- COMPARISON OF PREDICTED AND MEASURED SIDE FORCE AND YAWING MOMENT
COEFFICIENTS FOR V/STOL CONFIGURATIONS AT $\alpha = 35^\circ$ FOR ZERO SIDESLIP

Effect of Initial Asymmetry

Tail	Strakes		Data	C_Y		Data	C_n	
				$\Delta\beta=-1/2$	$\Delta\beta=2$		$\Delta\beta=-1/2$	$\Delta\beta=2$
Off	Off	Nose		-.012	-.000		-.010	-.001
		Wing/Body		-.009	-.089		-.002	+.060
		Tail		0	0		0	0
		Sum	-.034	-.041	-.089	-.012	-.012	+.059
Off	On	Nose		-.012	-.001		-.006	-.001
		Wing/Body		-.002	-.099		-.007	+.022
		Tail		0	0		0	0
		Sum	-.03	-.014	-.100	+.001	-.013	+.021
On	Off	Nose		-.032	0		-.010	-.001
		Wing/Body		-.010	-.148		-.002	+.006
		Tail		-.118	+.027		+.082	-.019
		Sum	-.04	-.180	-.121	-.01	+.070	-.014
On	On	Nose		-.012	-.001		-.006	-.001
		Wing/Body		-.007	-.029		-.003	+.003
		Tail		-.075	+.007		+.052	-.005
		Sum	-.048	-.094	-.023	+.012	+.043	-.003

Wing-Strake Vortex Initially at $z_i = 4$

Off	On	Nose		-.012			-.006
		Wing/Body		-.03			+.011
		Tail		0			0
		Sum	-.03	-.042		+.001	+.005
On	On	Nose		-.012			-.006
		Wing/Body		-.011			-.001
		Tail		-.016			+.011
		Sum	-.048	-.039		+.012	+.004

Nose Vorticity Fitted with 6 Vortices

Off	Off	Nose		-.032			-.010
		Wing/Body		+.004			-.001
		Tail		0			0
		Sum	-.034	-.028		-.012	-.011
On	Off	Nose		-.032			-.010
		Wing/Body		+.005			-.002
		Tail		-.061			+.042
		Sum	-.04	-.088		-.010	+.030

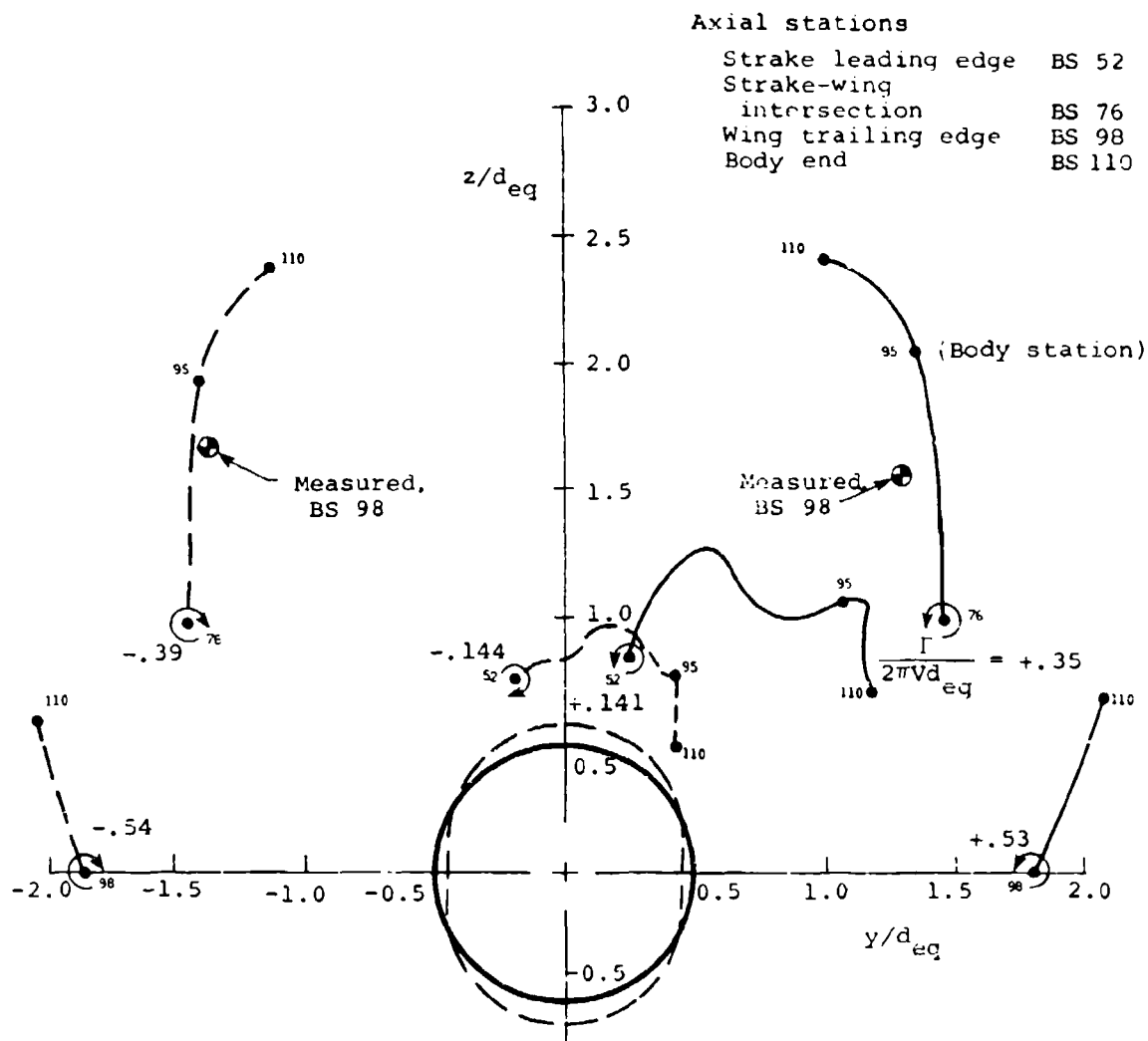


Figure 20. Predicted vortex positions over length of V/STOL model for $\alpha = 35^\circ$, $\beta = 0^\circ$, $\Delta\beta = -1/2^\circ$, strakes on.

Considering first the "standard" case, the nose, although it is the source of all the lateral effects, does not dominate the forces and moments. The forces on the wing/body portion are the smallest of the contributions and the tail forces are substantially larger than the nose force contribution. The predicted and measured values have the same trend and levels except for the case of tail on and strakes off. In this case, a large predicted interference load on the tail occurs which dominates the total predicted force and moment. An examination of the flow field data at the wing trailing edge (BS 98) shows a large separated wake region due to the wing without strakes, with axial velocities at the tail location about half that of the free stream. The dynamic pressure is then one quarter that of the free stream, rather than the free stream value assumed in the calculations. This effect would reduce the tail contribution to a quarter that shown in Table I, which would considerably improve the agreement for that case. With strakes to energize the flow over the wing, the measured axial velocities at the tail range from 10 percent less than free stream to 25 percent greater than free stream. Thus, the strakes have a very beneficial effect only on the high-angle longitudinal aerodynamics but on the control effectiveness of the vertical tail as well.

The results with the 2-degree disturbance on the nose show lower nose forces but greater wing/body interference forces and tail forces of opposite sign, compared to the "standard" case. Generally, the predicted results do not agree as well with the data, but no conclusive statements are possible. The results do indicate the sensitivity of the wing/body and tail interference loads to the nose vortex system.

The results for the six nose-vortex fit for the strake-off case are shown in Table I for comparison with the "standard" case. The direction of the side force induced on the wing/body is opposite that of the "standard" case and about half the magnitude. The vortex-induced tail side force is the same direction and about half the magnitude. The total loads compare more favorably with the measured values in general than do those of the "standard" case, again considering the tail q effect noted previously for the tail-on case. It is clear from these comparisons that a more detailed modeling of the nose vorticity distribution is desirable, with consideration of the entire cloud as the ultimate objective.

The final comparison shown in Table I is that of initial strake vortex height. The results for both tail-on and tail-off with the initial strake vortex height half that given by the delta wing data indicate generally better agreement with the data than do the "standard" results.

Consider now the results at 10 degrees of sideslip and 35 degrees angle of attack. Figure 21 shows predicted vortex positions over the length of the wing/body for the strake-off case. A four-vortex model is used to fit the nose vortex cloud. All four vortices move away from the body generally in the crossflow direction with increasing distance downstream. Figure 22 shows a measured circulation distribution above the body at the wing trailing-edge station (BS 98), which can be compared qualitatively with the predicted vortex positions at BS 98 from figure 21. There is a region of high measured positive circulation 3 to 4 diameters above the body which corresponds to the predicted position of the upper positive vortex in figure 21. To the left of this region are areas of only small measured circulation, which corresponds to the predicted positions of the lower positive and upper negative vortices in figure 21, which have a small negative combined strength. In general, the qualitative aspects of both the measured circulation distribution and the predicted concentrated vortices are reasonably similar.

For the case with strakes (fig. 23), the strake vortex heights were started at half the height indicated by the delta wing data, and their positions agree well with the measured core positions at the wing trailing edge (BS 98). The nose vortex cloud is fitted with a three-vortex system. All three vortices tend to rise under free stream influence until the strake vortices are introduced into the flow. Since the strengths of the strake vortices are several times those of the nose vortices, the strake vortices begin to force the nose vortices down. Again the strake vortices so dominate the measured circulation at the wing trailing edge that there is no possibility of identifying the nose vorticity and comparing its position with the predicted vortex position.

The predicted and measured loads on the V/STOL model with and without vertical tail and strakes at 10 degrees of sideslip are shown in Table II. The predicted side forces are in the same direction as the measured values, but are considerably smaller in magnitude than the measured values. The yawing moments are also too small in magnitude.

TABLE II

COMPARISON OF PREDICTED AND MEASURED SIDE FORCE AND YAWING
MOMENT COEFFICIENTS FOR V/STOL CONFIGURATIONS
 $\alpha = 35^\circ$ FOR 10° SIDESLIP

<u>Tail</u>	<u>Strakes</u>		<u>Data</u>	<u>C_y</u>	<u>Data</u>	<u>C_n</u>
				<u>Theory</u>		<u>Theory</u>
Off	Off	Nose		-.044		-.02
		Wing/Body		-.018		+.008
		Tail Dir		0		0
		Tail Intf		0		0
		Sum	-.17	-.062	-.046	-.012
Off	On	Nose		-.019		-.016
		Wing/Body		-.033		+.013
		Tail Dir		0		0
		Tail Intf		0		0
		Sum	-.12	-.052	-.068	-.003
On	Off	Nose		-.004		-.02
		Wing/Body		-.007		-.000
		Tail Dir		-.08		+.005
		Tail Intf		+.023		-.016
		Sum	-.216	-.108	-.038	+.019
On	On	Nose		-.019		-.016
		Wing/Body		-.021		+.005
		Tail Dir		-.080		+.005
		Tail Intf		+.077		-.054
		Sum	-.136	-.043	-.06	-.010

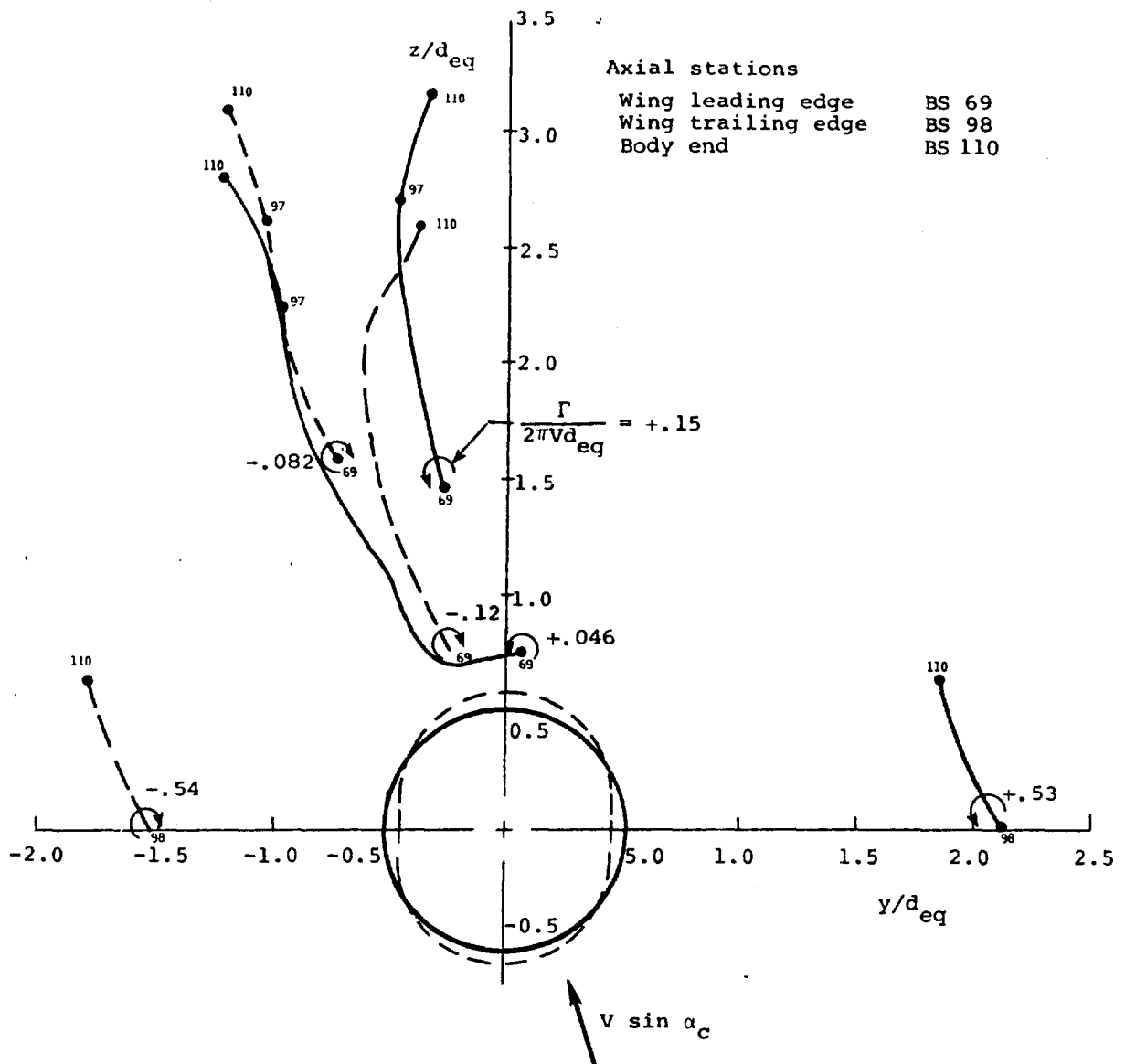


Figure 21. Predicted vortex positions over length of V/STOL model for $\alpha = 35^\circ$, $\beta = 10^\circ$, strakes off.

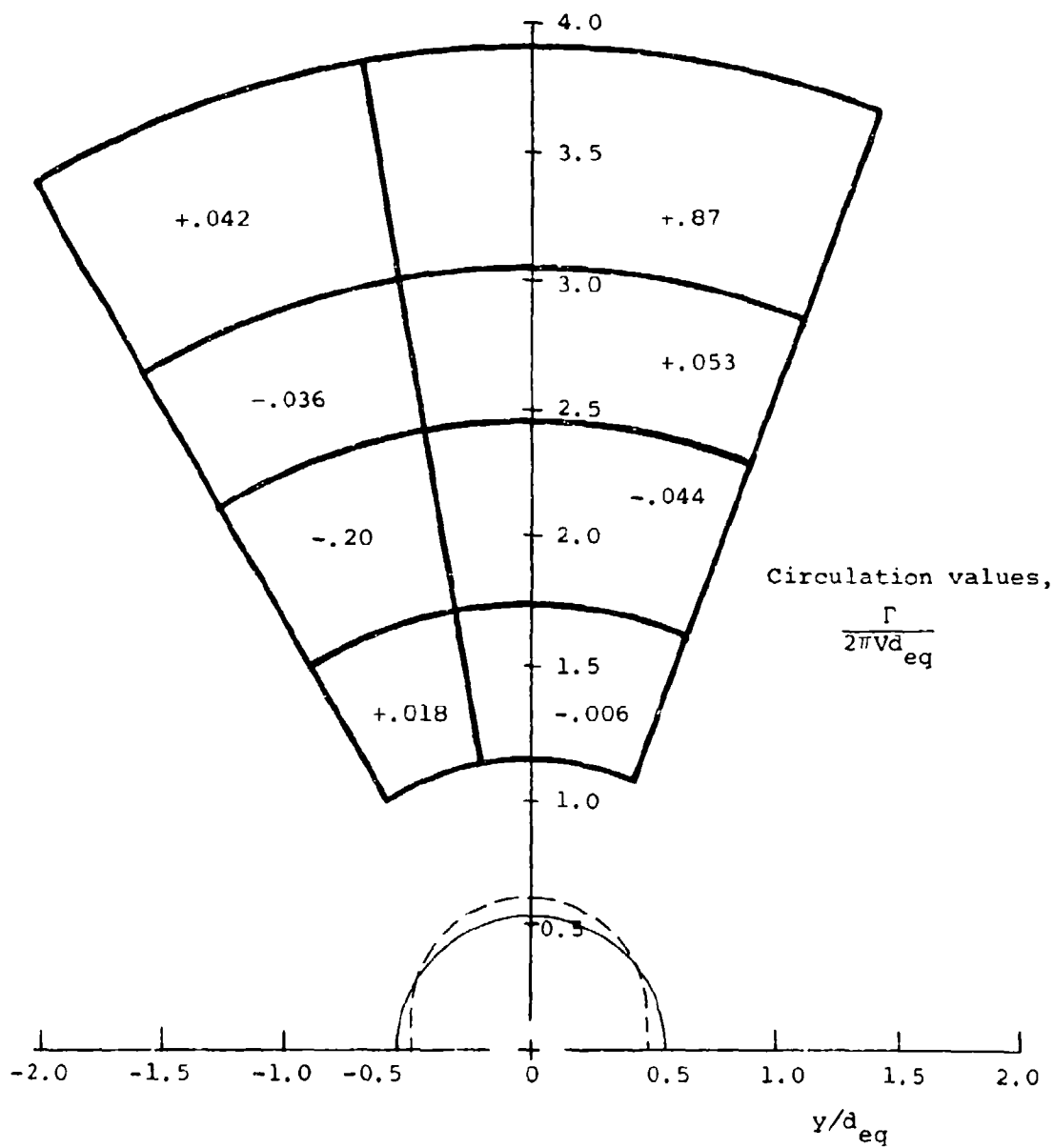


Figure 22. Measured circulation distribution over V/STOL body at wing trailing edge (BS 98) for $\alpha = 35^\circ$, $\beta = 10^\circ$, strakes off.

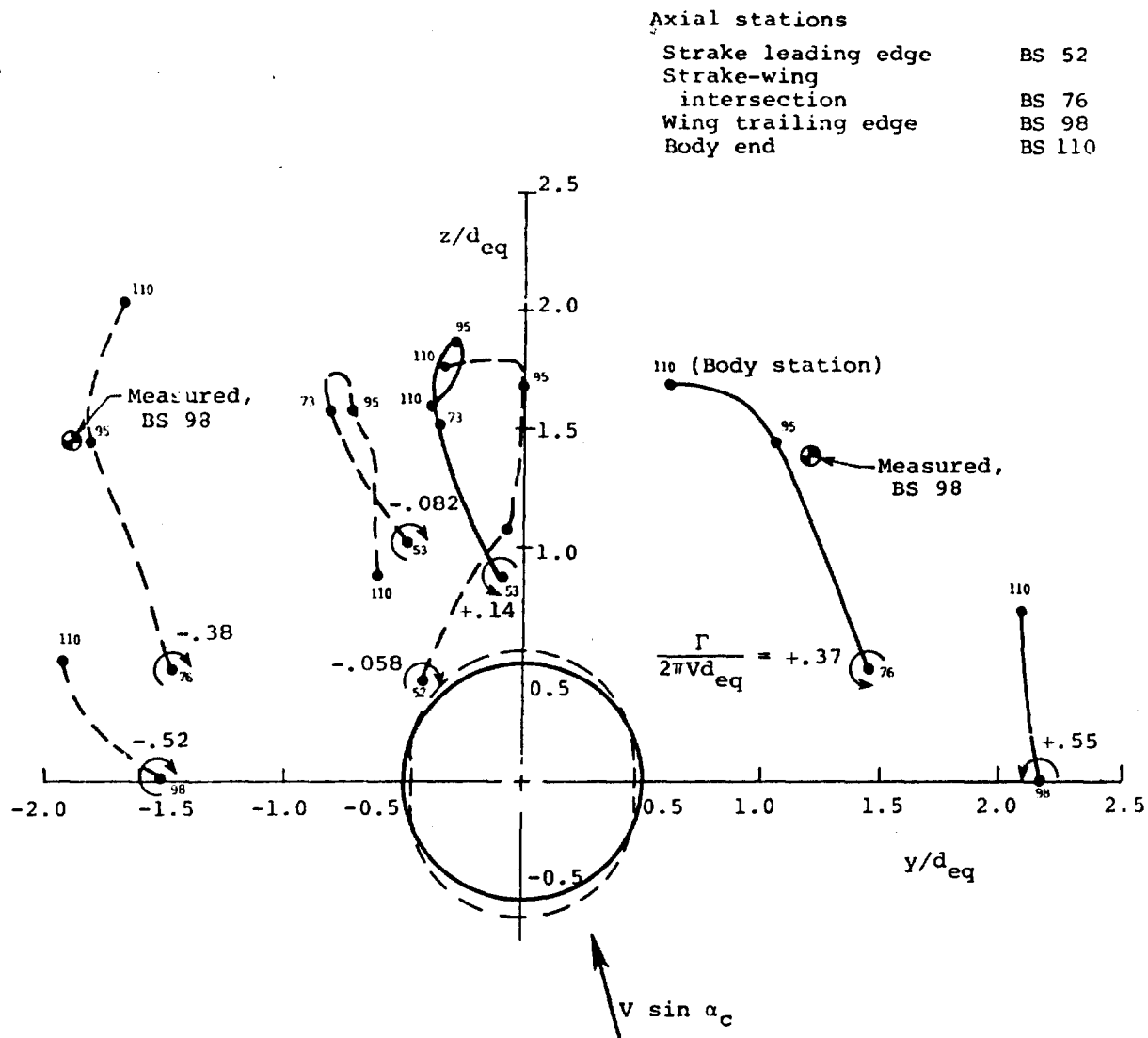


Figure 23. Predicted vortex positions over length of V/STOL model for $\alpha = 35^\circ$, $\beta = 10^\circ$, strakes on.

In order to have better agreement on both side force and yawing moment, a larger negative nose side force is required. The predicted nose-alone side force agrees well with water tunnel data (fig. 12), although the Reynolds number was only half that of the wind tunnel tests. Since no breakdown of forces on the model is available from the wind tunnel tests, the source of the differences cannot be identified.

It is interesting to note that without strakes the predicted tail interference force is a small part of the no-interference tail force, whereas with strakes, the tail interference forces essentially offset the direct tail load.

For this model, the yawing moments produced at $\alpha = 35^\circ$ are destabilizing for all the configurations shown in Table II.

5.2.2 F-5A model.— Since no flow visualization or flow field data are available for the F-5A, only the overall loads are compared with predictions. The results are shown in Table III for angles of attack of 30° and 40° and sideslip angles of 0° and 10° .

The division of predicted loads between nose, wing-body, afterbody, and tail is shown, together with their sum and the measured overall value from reference 11. Generally, the loads on each component are appreciable and have differing signs, so the sum is about the same magnitude as the individual components. For the two cases with sideslip, the vortex interference forces on the tail are comparable to the direct loads on the tail due to sidewash, and effectively negate the stabilizing direct tail contribution to the yawing moment.

Generally, all measured and predicted results agree qualitatively except the $\alpha = 30^\circ$, $\beta = 10^\circ$ case. For this condition, the source of difference in sign of the measured and predicted force and moment is very probably an underprediction of tail vortex interference load. The nose-alone data of reference 11 show a small negative side force on the nose, whereas the prediction gives a small positive side force. With this correction for the nose, the predicted total side force would be more negative, and the only major source of a positive side force which would cause better agreement on total force is the tail interference force. For the other three flow cases shown in Table III, a change in the tail vortex interference side force to cause better agreement with total side force would also cause better agreement with total yawing moment, whereas

TABLE III

COMPARISON OF PREDICTED AND MEASURED SIDE FORCE
AND YAWING MOMENT COEFFICIENTS FOR F-5A

	<u>$\alpha = 30^\circ, \beta = 0^\circ$</u>		<u>$\alpha = 40^\circ, \beta = 0^\circ$</u>	
	C_Y	C_n	C_Y	C_n
Nose	-.017	-.026	-.063	-.026
Wing/Body	-.006	-.004	-.015	-.028
Afterbody	+.027	0	+.077	-.100
Tail	<u>+.033</u>	<u>-.053</u>	<u>-.090</u>	<u>-.144</u>
Sum	+.037	-.113	-.153	-.010
Measured	+.010	-.083	-.062	-.069
	<u>$\alpha = 30^\circ, \beta = 10^\circ$</u>		<u>$\alpha = 40^\circ, \beta = 10^\circ$</u>	
	C_Y	C_n	C_Y	C_n
Nose	+.018	+.027	+.072	+.128
Wing/Body	+.041	+.016	+.009	+.026
Afterbody	+.047	-.052	+.042	-.045
Tail Dir	-.444	+.709	-.444	+.709
Tail Intf	<u>+.283</u>	<u>-.452</u>	<u>+.499</u>	<u>-.797</u>
Sum	-.055	+.248	+.172	+.017
Measured	+.016	-.046	+.122	+.112

a change in nose force would not improve yawing moment. The problem in these cases is probably the way in which the nose vortex cloud is fitted with discrete vortices, which influences the way in which these vortices move back over the tail and the load induced on the tail, and/or vortex bursting, at least at $\alpha = 40^\circ$.

6. DISCUSSION OF RESULTS

Several aspects of the physics of the flow, the calculations, and comparisons with data are worthy of discussion. These include vortex bursting, sensitivity of the results to separation location on the nose, vortex tracking, and modeling of the nose vortex cloud.

Vortex bursting is known to occur on highly swept wing and wing-strake configurations at high angles of attack (for instance, refs. 12 and 13). Bursting occurs first aft of the trailing edge and moves forward over the wing as the angle of attack increases. The occurrence of bursting will have an influence on the load distribution on the wing and fuselage (ref. 12), although few detailed experimental data are available for fighter aircraft configurations. No indications of bursting are present in the existing data on body or nose vortices.

The flow field data presented in reference 3 show axial velocities in the cores of the nose vortices at stations BS 52 and 69 which are typically 25 percent higher than those of the surrounding flow. Although it is difficult to identify the nose vortices in the flow field measurements at the wing trailing edge (BS 98), for the case of strakes off, there are small areas that have high axial velocities and also high local circulation and would appear to be the nose vortices.

With strakes on, the wing trailing-edge flow-field data show regions in the cores of the strake vortices with essentially zero axial velocity. Since measurements were taken only at one axial station over the wing, it is difficult to say where strake vortex bursting occurs, but it appears to have occurred at or upstream of the trailing edge.

Vortex bursting is not included in the analytical methods nor the predicted loads. While a reasonable amount of work has been done on lifting surfaces having burst vortices (mostly delta wings), the mechanism of bursting is not completely understood, and no reliable prediction

methods for burst locations are available, particularly for more complex configurations with breaks in leading edge sweep and bodies. What is perhaps equally important is that no work has been done on developing a model to predict the induced velocities on adjacent lifting surfaces caused by a burst vortex, which probably retains its overall circulation but with a much more diffuse distribution. The probable influence of this phenomenon on the comparisons given in the preceding section is difficult to assess.

One factor that was discussed in the section on nose data comparisons is the location of the predicted separation points on the nose (fig. 13). The Stratford criteria are empirical correlations for a two dimensional flow that were derived from flat plate data. In earlier work done under this contract (ref. 3), the criteria were applied to two dimensional flows over cylinders and ellipses where other theoretical methods and data are available and were found to agree well with the other sources. Limited comparisons were made with three dimensional separation line data on inclined ogive-cylinders, and the " $\sin \alpha$ " correction was deduced based on these comparisons. The modified Stratford criteria are considered preliminary at this time, which is the reason why the calculations typified by figure 13 were done.

The difficulty noted in connection with figure 13 was found with both the V/STOL and F-5 nose shapes. In the latter case, there are relatively flat sections on the side of the nose near the rear which have small circumferential pressure gradients subject to local changes due to the presence of adjacent vortices in the cloud. These changes can cause the separation point to move circumferentially from one axial station to the next, which changes the point where the vortex is inserted in the flow field and tends to disturb the orderly movement of vortices into the lee side flow field. In some cases the (axially) downstream influence of variations in separation location damps out and does not appear to influence the loads or vorticity distribution. In other cases the disturbance tends to cause such events as driving a vortex towards the body where its motion is then dominated by its image which forces the vortex down along the body surface towards the windward side.

Some additional work needs to be done to evaluate and perhaps modify the separation criteria used in the nose separation program. It would be desirable to make more comparisons with separation line location data for

circular and for noncircular cross section bodies inclined at various angles to the flow. Based on the comparisons, a set of criteria should be established which not only reflects the circumferential pressure gradients imposed on the boundary layer but the axial run lengths as well. This work could well eliminate the problem associated with flat regions of very low pressure gradients. If not, special provisions could be made in the computer program to handle this case, again based on placing the separation point properly as indicated by appropriate data.

The predicted results for complete configurations show appreciable loads on the vertical tail due to the nose vortices. The tail loads depend on the way in which the nose vortex cloud is modeled with a few discrete vortices, the vortex tracking method, and the tail load calculation method. The latter two methods have been used for many years in connection with wing/body/tail interference calculations and have been validated through comparisons with data on vortex positions and panel loads, at least for circular bodies. The differences for the present calculations not generally encountered in most missile and aircraft cases are the noncircular bodies approximated by circular bodies having the same cross section area distribution and the low wing (in the F-5) approximated by a midwing in the vortex tracking calculation. These approximations will have some influence on tail loads, but the errors involved are probably small compared to differences between predicted and measured loads.

The way in which the nose vortex cloud is modeled with several discrete vortices can cause an appreciable effect on the predicted tail loads. Figure 18 shows a comparison of a 2 and a 6 vortex fit to a nose vortex cloud which indicates quite different distributions of vortices at the tail location. Table I shows a factor of two difference in the vortex-induced tail loads between these two cases, with the six-vortex fit giving better agreement with data. No systematic investigation was made of this matter because the vortex tracking program used to locate the vortices over the body length was held to twelve nose and wing vortices to minimize program running time. It would be desirable to modify the computer program to be able to track the entire cloud of vortices aft to the tail, so a systematic study could be made of simpler representations of the nose vortex system which retains the necessary accuracy in vorticity distribution and induced velocity field.

Finally, notice should be taken of the V/STOL model experimental results regarding the importance of strakes in energizing the flow at the tail. The probe velocity measurements at the wing trailing edge indicate little loss in axial velocity from the free stream value ($V_{\infty} \cos \alpha$) with strakes but a loss of half the free stream component (and three-quarters of the dynamic head) without strakes. This effect occurs even though the data indicate the strake vortices to be burst at the wing trailing edge at $\alpha = 35^\circ$. Thus the strake vortices play an important role in influencing dynamic pressure at the tail at angles of attack for which leading edge separation occurs on the wing.

7. CONCLUDING REMARKS

A theoretical and experimental study has been conducted to develop analytical techniques for predicting the lateral aerodynamic loads on fighter-type aircraft at high angles of attack that influence departure. The experimental work was done both in NEAR and NASA facilities and was designed to provide specific, detailed data to support development of the analytical methods.

Analytical methods were developed to predict loads on all components of a typical aircraft configuration. The most important of these is a method to predict the pressure distribution, location of separation, and vorticity field in the wake of an arbitrarily shaped, noncircular cross section nose. The noncircular nose shapes used on modern fighter aircraft play a very significant role in the high angle-of-attack handling qualities of the aircraft, and the method developed in this work is the only existing method capable of treating such shapes. Furthermore, the flow field measurements obtained at Langley Research Center are the first such measurements obtained on a noncircular cross section, fighter-type configuration and were extremely useful in evaluating the analytical methods.

The results of data comparisons both on noses alone and on complete configurations show the correct qualitative behavior and in many cases show good quantitative agreement. However, the comparisons are not sufficiently consistent in prediction of magnitudes of forces to be considered reliable design or analysis techniques. Additional work is

needed in data comparisons to validate completely, and perhaps improve, the flow models. The critical data required, for the most part, do not exist, and some additional experiments are desirable.

In particular, the kinds of measurements that need to be made are flow field, pressure distribution and flow separation location data on noncircular nose shapes of interest to modern fighter aircraft, vortex flow field measurements on complete configurations to define the locations of vortices, their burst points, vorticity distributions, and induced flow fields, and breakdown of loads on complete configurations. Attention also needs to be given to prediction of burst points for strake and hood vortices and the induced velocity fields of burst vortices, with such analysis supported by critical experiments.

REFERENCES

1. Spangler, S. B. and Nielsen, J. N.: Exploratory Study of Aerodynamic Loads on a Fighter-Bomber at Spin Entry. NEAR TR 87, May 1975.
2. Spangler, S. B. and Dillenius, M. F. E.: Investigation of Aerodynamic Loads at Spin Entry. Report ONR-CR212-225-2, May 1976.
3. Spangler, S. B. and Mendenhall, M. R.: Further Studies of Aerodynamic Loads at Spin Entry. Report ONR-CR212-225-3, June 1977.
4. Polhamus, E. C.: Predictions of Vortex Lift Characteristics by a Leading-Edge Suction Analogy. J. of Aircraft, Vol. 8, No. 4, April 1971.
5. Deffenbaugh, F. D. and Koerner, W. G.: Asymmetric Wake Development and Associated Side Forces on Missiles at High Angles of Attack. AIAA Paper No. 76-364, July 1976.
6. Jameson, A.: Iterative Solution of Transonic Flows over Airfoils and Wings, Including Flows at Mach 1. Comm. Pure & Appl. Math., Vol. 27, 1974, pp. 283-309.
7. Stratford, B. S.: The Prediction of Separation of the Turbulent Boundary Layer. J. of Fluid Mech., Vol. 5, 1959, pp. 1-16.
8. Mendenhall, M. R. and Nielsen, J. N.: Effect of Symmetrical Vortex Shedding on the Longitudinal Aerodynamic Characteristics of Wing-Body Combinations. NASA CR-24,2, January 1975.
9. DeYoung, J. and Harper, C. W.: Theoretical Symmetric Span Loading at Subsonic Speeds for Wings Having Arbitrary Planform. NACA Rept. 921, 1948.

10. Pitts, W. C., Nielsen, J. N. and Kaattari, G. E.: Lift and Center of Pressure of Wing-Body-Tail Combinations at Subsonic, Transonic, and Supersonic Speeds. NACA Rept 1307, 1959.
11. Grafton, S. B., Chambers, J. R. and Coe, P. L.: Wind Tunnel Free-flight Investigation of a Model of a Spin Resistant Fighter Configuration. NASA TN D-7716, June 1974.
12. White, R. P., Gangwani, B. T. and Balcerak, J. C.: A Theoretical and Experimental Investigation of Vortex Flow Control for High Lift Generation. Report ONR-CR212-223-3, December 1976.
13. Titirigi, A., Skow, A. M. and Moore, W. A.: Forebody/Wing Vortex Interactions and Their Influence on Departure and Spin Resistance. AGARD Meeting on High Angle of Attack Aerodynamics, October 4-6, 1978.

SYMBOLS

C_n	yawing moment coefficient, nondimensionalized by base area and equivalent base diameter for noses alone, wing area extended to model centerline and wing span for V/STOL aircraft, and basic wing area extended to centerline and mean aerodynamic chord for F-5 aircraft
C_p	pressure coefficient, $(p-p_\infty)/q$
C_Y	side force coefficient, nondimensionalized by base area for noses alone and wing area extended to centerline for complete configurations
d_{eq}	diameter of a circle having same cross section area as base of body
L_n	nose length
q	free stream dynamic head, $\frac{1}{2}\rho V^2$
Re_D	Reynolds number, VD/ν
Re_s	Reynolds number, Vs/ν
s	distance in crossflow-plane along body surface from virtual origin
S_b	base area of body
u, v, w	velocity components along x, y, z directions, respectively
u_δ	boundary layer edge velocity
V	free stream velocity
x, y, z	coordinate system with origin at nose, x aft body axis, y to right, and z vertical upwards
y_v, z_v	coordinates of vortex in crossflow plane
z_i	initial height of strake vortex at strake-wing intersection
α	angle of attack
α_c	included angle between velocity vector and body axis for combined angles of attack and sideslip
β	angle of sideslip
$\Delta\theta$	shift of two separation angles in crossflow plane used to induce asymmetry in nose vortex shedding

SYMBOLS (Concluded)

Γ	vortex strength
ν	kinematic viscosity
ρ	free stream density
θ	polar angle in crossflow plane measured from negative z axis positive counterclockwise
θ_s	angle of separation

DISTRIBUTION LIST

Office of Naval Research 800 N. Quincy St. Arlington, VA 22217 ONR 211 ONR 430B	4 1	Naval Surface Weapons Center White Oak Laboratory Silver Spring, MD 20910 WA-41 (Mr. W. J. Yanta)	1
Office of Naval Research Branch Office 1030 E. Green St. Pasadena, CA 91106	1	U. S. Naval Postgraduate School Monterey, CA 93940 Dept. of Aeronautics (Code 57) Library	1 1
Office of Naval Research Branch Office Bldg. 114 Section D 666 Summer St. Boston, MA 02210	1	Superintendent U. S. Naval Academy Annapolis, MD 21402	1
Office of Naval Research Branch Office 536 South Clark St. Chicago, IL 60605	1	Air Force Office of Scientific Research Bolling AFB, DC 20332 Code NA (Dr. J. Wilson)	1
Naval Research Laboratory Washington, DC 20375 Code 2627 Code 2629	1 1	Air Force Flight Dynamics Laboratory Wright Patterson AFB, OH 45433 AFFDL/FGC (Mr. D. Bowser) AFFDL/FGC (Mr. E. Flinn) AFFDL/FGC (Mr. R. Woodcock) AFFDL/ASD (Mr. R. Weissman) AFFDL/FGL (Mr. P. Blatt) AFFDL/FXM (Mr. R. Jeffries) AFFDL/FXM (Mr. R. Osborn)	1 1 1 1 1 1 1
Defense Documentation Center Bldg. 5, Cameron Station Alexandria, VA 22314	12	U. S. Army Missile R&D Command Redstone Arsenal, AL 35809 DRDMI/TDK (Mr. D. J. Spring)	1
Naval Air Systems Command Washington, DC 20361 AIR 320D (Mr. R. Siewert)	1	Arnold Engineering Development Center Arnold AFS, TN 37389 Mr. R. Butler Mr. F. Langham Mr. T. Perkins Mr. A. Money	1 1 1 1
Naval Air Development Center Warminster, PA 18974 Code 6053 (Dr. K. T. Yen) Code 6053 (Mr. C. Henderson)	2 1	Defense Advanced Research Projects Agency 1400 Wilson Boulevard Arlington, VA 22209 Mr. R. Moore	1
David Taylor Naval Ship Research and Development Center Bethesda, MD 20084 Code 16 (Dr. H. Chaplin) Code 522.3 Aero Library Code 1660 (Mr. J. Nichols)	1 1 1	NASA Langley Research Center Hampton, VA 23365 MS 286 (Mr. R. Margasson) MS 287 (Dr. J. Campbell) MS 343 (Mr. J. Bowman) MS 355 (Mr. J. Chambers) MS 355 (Mr. W. Gilbert) MS 355 (Mr. E. Anglin) MS 208 (Mr. P. Bobbit) MS 287 (Mr. E. Pulhamus)	1 1 1 1 1 1 1
Naval Weapons Center China Lake, CA 93555 NWC-3914 (Mr. W. H. Clark) NWC-3209 (Mr. R. W. Van Aker)	1 1		

NASA Ames Research Center		General Dynamics	
Moffett Field, CA 94035		Convair Division	
MS 227-8 (Mr. G. Chapman)	1	P. O. Box 80847	
MS 227-8 (Mr. G. Malcolm)	1	San Diego, CA 92136	
MS 227-8 (Mr. L. Presley)	1	Dr. E. Levinsky	1
NASA Dryden Flight Research Center		Boeing Aircraft	
Edwards AFB, CA 93523		P. O. Box 3707	
Mr. P. Carr	1	Seattle, WA 98124	
Mr. W. Dana	1	Dr. P. Rubbert	1
Mr. E. Enevoldsen	1	Virginia Polytechnic Institute & State	
Mr. D. Lux	1	University	
Mr. T. Ayers	1	Engineering Science Dept.	
Lockheed Missiles & Space Co., Inc.		Blacksburg, VA 24061	
Huntsville Research & Engineering		Dr. D. Mook	1
Center		Royal Aircraft Establishment	
P.O. Box 1103		Farnborough Hants	
Huntsville, AL 35807		United Kingdom	
Mr. A. Zalay	1	Mr. G. Moss	1
McDonnell Douglas Aircraft Company			
P. O. Box 516			
St. Louis, MO 63166			
Dept. 230 (Mr. R. W. McDonald)	1		
Dept. 241 (Mr. R. B. Jenny)	1		
(Mr. D. Kotansky)	1		
Vought Corporation			
Advanced Technology Center, Inc.			
P. O. Box 6144			
Dallas, TX 75222			
Dr. Gary Hough	1		
Grumman Aerospace Corporation			
Bethpage, NY 11714			
Research Dept. (Dr. R. Melnik)	1		
Rockwell International			
Columbus Aircraft Division			
Columbus, OH 43216			
Research Dept. (Dr. P. Bevilacqua)	1		
Northrop Corporation			
Aircraft Division			
3901 W. Broadway			
Hawthorne, CA 90250			
Mr. Gordon Hall	1		
Mr. A. Skow	1		
Northrop Corporation			
Ventura Division			
1550 Rancho Conejo Blvd.			
Newport Park, CA 91320			
Dr. A. Wortman	1		